University of Wrocław (PL)

Faculty of Physics and Astronomy

CERN (CH)

NA61/SHINE Experiment

Pulser Calibration of Time Projection Chambers in the NA61/SHINE Experiment

Author:
Maciej Lewicki

Supervisor:
Dr Thomas Klähn

November 5, 2015

Abstract

This study aimed at developing a method for *pad-by-pad* pulser calibration of Time Projection Chambers (TPCs) for the CERN experiment NA61/SHINE.

The research consists of three main parts: data gathering, software development and thorough testing. The first and the second section were performed under the wardship of Dr Andras Laszlo at CERN's Prevessin site North Area in November and December of 2014. The calibration routine was later tested and adjusted to achieve the highest possible precision.

The resulting product of my work is firstly a reliable algorithm included to experiment software framework SHINE and secondly the set of time delay and electronic gain correction factors for all TPCs. The experimental data collected by the NA61's detectors would benefit from an increased spatial resolution and total charge calculation, which would result with in a more reliable particle identification.

Tytuł:

Klaibracja Komór Projekcji Czasowej w Eksperymencie NA61/SHINE Przy Użyciu Pulsera

Streszczenie

Badania opisane w tej pracy zostały przeprowadzone w celu stworzenia nowej metody kalibracji Komór Dryfu w eksperymencie NA61/SHINE o środku CERN.

Wykonana praca badawcza składa się z trzech głównych części: zbieranie danych, tworzenie oprogramowania i rygorystyczne testowanie. Pierwsze dwa etapy zostały wykonane pod okiem dra Andras'a Laszlo w listopadzie i grudniu 2014 roku, w tzw. "North Area" w Prevessin, w CERN'ie. Stworzone oprogramowanie było następnie testowane i modyfikowane w celu otrzymanie najwyższej możliwej precyzji.

W rezultacie stworzony został sprawdzony algorytm, wciągnięty do platformy oprogramowania eksperymentu SHINE oraz pełna lista współczynników poprawek na opóźnienia czasowe oraz intensywność sprzęgania elektroniki dla każdej z komór. Współczynniki te wniosą istotną poprawkę do jakości zbieranych danych: poprawią przestrzenną zdolność rozdzielczą detektora, a także zdolność obliczania strat energii, która z kolei wpływa bezpośrednio na jakość identyfikacji cząstek.

Keywords:

Heavy-Ion Collisions, Time Projection Chamber, NA61/SHINE, CERN, calibration

Contents

Part I

Introduction

1 Preface

This study is a tiny part of the detector calibration procedure used in the NA61/SHINE data acquisition and analysis. Which is an even tinier fraction of a huge effort of circa 150 physicists involved in the collaboration. The motivation of this work is to improve the measurements resolution for the largest sub-detector of the experiment – the Time Projection Chambers. The improvement will be mostly noticeable in a precision of spatial measurements, but will also contribute to charge deposition calculations. This will lead to a slightly increased precision of finding particles' track topology and energy loss, which will finally contribute to a more reliable particle identification.

In the first part of this thesis I will focus on the NA61/SHINE experiment – the physics behind, its research goals and the detector system. Later on I will describe in detail the calibration routine I developed. In the final part I will discuss the results of the calibration in terms of reliability and performance.

2 NA61/SHINE experiment

The SPS Heavy Ion and Neutrino Experiment – NA61/SHINE is a particle physics experiment nested at European Organization for Nuclear Research (CERN). The experiment operates using proton and ion beams produced at the Super Proton Synchrotron and sent to the CERN's North Area. The beam is directed at a fixed target of various materials and the effects of caused collisions are observed with a large acceptance hadron spectrometer. The experiment studies the production of hadrons at the edge between baryonic matter and its deconfined state, the so called Quark Gluon Plasma. [1]

3 Theoretical background

3.1 Quantum Chromodynamics

The theoretical background behind the NA61/SHINE experiment is given by the strong interaction theory called Quantum ChromoDynamics (QCD) – a non-Abelian gauge theory of quarks, with gluons as mediators, with the $SU(3)$ symmetry group. The description of states of matter according to QCD uses two external thermodynamic parameters: the temperature T and the baryochemical potential μ_B. Those two parameters span the plane (T, μ_B) being the phase-diagram of the states of matter in QCD. Each point on the diagram corresponds to a stable thermodynamic state with certain thermodynamic functions assigned: pressure, baryon density, etc.

The full thermodynamic description of a state, from which the static quantities can be derived,

is given by the partition function [2]:

$$\mathcal{Z}(T, \mu_B) = \sum_\alpha \exp\left(-\frac{E_\alpha - \mu_\alpha B_\alpha}{T}\right) = \int \mathcal{D}(A, q, q^*) \exp(-S_E)$$

The partition function Z is given as the Gibbs sum over Hamiltonian eigenstates, where α denotes states with E_α energy and B_α baryon number. Such sum may also be expressed as a Euclidean path integral over color gauge (gluon) fields A_μ.

The Euclidean action in the equation above is given by:

$$S_E = S_{YM} + \sum_{q=u,d,s} \int d^4x \; q^\dagger \mathbb{D} q$$

where S_{YM} is Yang-Mills action,

the q are the Dirac spinors in the chiral Weyl basis: $q = \begin{pmatrix} q_L \\ q_R \end{pmatrix}$

and Dirac martix is given by:

$$\mathbb{D} = \begin{pmatrix} \sigma \cdot D & m_q \\ m_q \sigma^\dagger \cdot D \end{pmatrix} - \mu_B$$

where: $\quad \sigma\mu = (1, i\sigma), \quad D_\mu = \partial_\mu - iA_\mu, \quad \mu_q = \mu_B/3$

3.2 QCD properties

QCD derives two fundamental properties at opposite ends of the (T, μ_B) phase-diagram:

- **Confinement** – While in electrodynamics and gravity potential decreases with distance, it is not the case for QCD. Due to the fact that the force between quarks does not diminish with distance the **quarks cannot exist as free particles**. Increasing the distance between quarks causes the gluon field to reach the energy high enough for creation of another quark pair.

- **Asymptotic freedom** – At sufficiently high density or in a very high energy, namely:

$$\epsilon \sim 1 \text{ GeV/fm}^3, \quad T \sim 200 \text{ MeV}$$

  the hadrons start to interpenetrate and the strong interactions between quarks are suppressed. This leads to creation of weakly interacting soup of quarks and gluons, called **Quark-Gluon Plasma**.
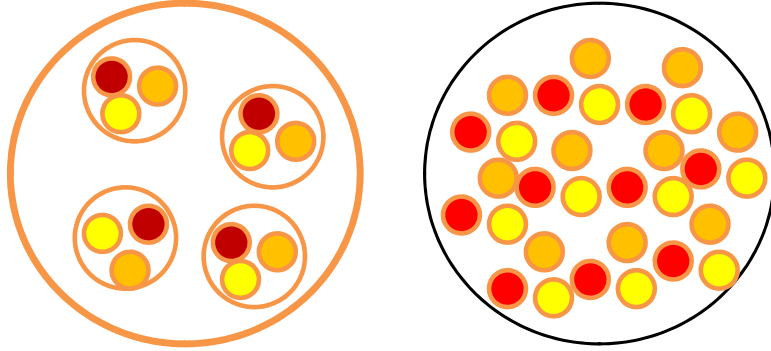
Figure 1: Left: hadronic matter as a nucleus at normal density.
Right: deconfined quark matter.
image credit: [3]

The reason of the existence of confined and deconfined states of matter was first explained by Wilczek, Poltzer and Gross (Nobel Prize in Physics 2004). They assumed the dependence of a coupling parameter α_s on the energy scale μ (the beta function) being negative:

$$\beta(\alpha_s) \quad = \quad \mu\frac{d\alpha(\mu)}{d\mu} \quad = \quad -\frac{\beta_0}{2\pi}\alpha^2 + \cdots$$

where $\beta_0 = 11 - \frac{2n_f}{3}$. The first term, 11, comes from gluon contribution and the second term, $-\frac{2n_f}{3}$, comes from quark-antiquark pairs.
Now one can approximate the QCD coupling constant becomes:

$$\alpha_s(\mu) = \frac{2\pi}{\beta_0 \ln(\mu/\Lambda_{QCD})}$$

As a result the coupling constant decreases logarithmically towards high energies and small distances, which is exactly the phenomenon introduced already as the asymptotic freedom. On the other hand, at low energies, the coupling becomes large and excludes the usage of the perturbation theory.
The value Λ_{QCD} in the equation above is the only independent scale in QCD:

$$\Lambda_{QCD} \sim 1fm^{-1}$$

.

3.3   Phase transition and critical point

The chiral limit sets the idealized condition on quark mass – the lightest quarks: u and d are taken to be massless. Such feature causes the Lagrangian to acquire the chiral $SU(2)_L \times SU(2)_R$

symmetry, which corresponds to $SU(2)$ flavour rotations on doublets (u_L, d_L) (u_R, d_R) independently. The ground state of QCD in such conditions spontaneously breaks the symmetry, generating 3 massless Goldstone bosons - the pions. On the other hand at the temperature high enough $T \gg \Lambda_{QCD}$, due to the asymptotic freedom, the approximation of free quarks and gluons gas should become applicable. In this regime the chiral symmetry is not broken. Thus we expect to observe a phase transition, near the temperature $T \sim \Lambda_{QCD}$, from a broken chiral symmetry ground state to a chirally symmetric equilibrium phase. [4]

For two massless quarks the transition can be either second or first order. When masses of up and down quarks are set to their observed values we learn that the transition is actually a crossover in a low μ_B region, first order transition in higher μ_B and it features a second order critical point someplace in between. [5]
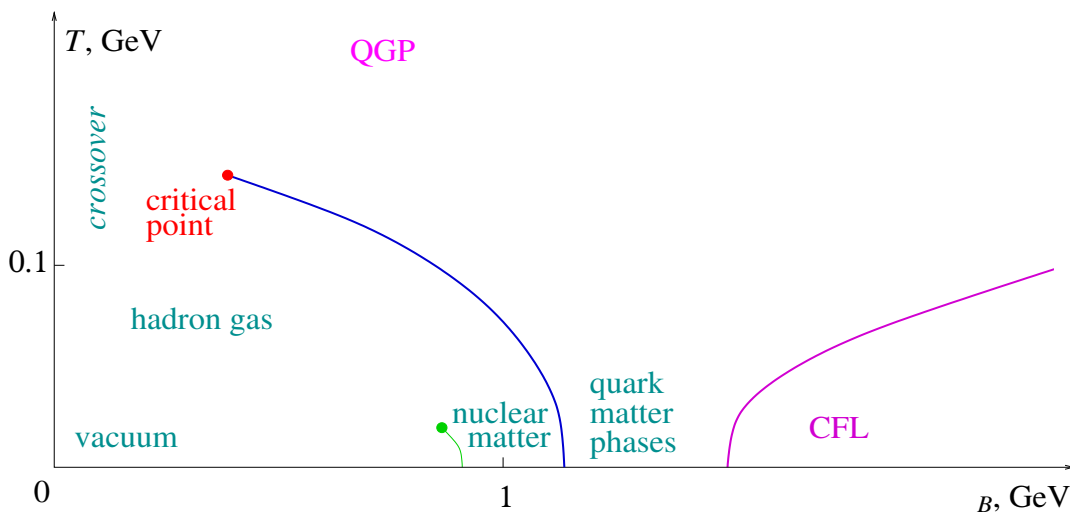
Figure 2: Semi-quantitative sketch of QCD phase diagram.
image credit: [2]

3.4 Finding the Critical Point

In order to find the critical point one needs to calculate the QCD partition function and find the singularity corresponding to the end of the first order transition line [2]. Such an approach seems pretty straightforward, but the $\mathcal{Z}$ function is in fact an infinitely dimensional integral, which calculation is far beyond present computational power. In a region of low μ_B the lattice Monte Carlo simulations are working very well, but outside that region two serious problems arise:

- **Sign problem**

  The exponent of the Euclidean action S_E is a positive-definite function. This allows using a method called *importance sampling*. It reduces the set of field configurations by randomly picking states with a probability proportional to $\exp(-S_E)$. Now in QCD, where $\mu_B \neq 0$ the action S_E is complex. There are numerous approaches of circumventing the problem, but none of the methods converges to correct result with an increasing

volume.

- **Overlap problem**
  Being unable to obtain a correctly weighted sample of configurations, one can try to extrapolate the probability from the well defined region with $\mu_B = 0$, so the contribution of each state is multiplied by a factor of $\exp(S_E|_{\mu_B=0} - S_E)$ [6]. This way the probability of some of the important configurations in $\mu_B \neq 0$ region drops significantly. Therefore the reweighting correction factor gets extremely large and amplifies any fluctuations and statistical noises. This way the obtained results are completely unreliable.

In the absence of reliable simulations of QCD at nonzero μ_B many model calculations have been performed. Figure below summarizes the results of the search for the critical point by various methods.
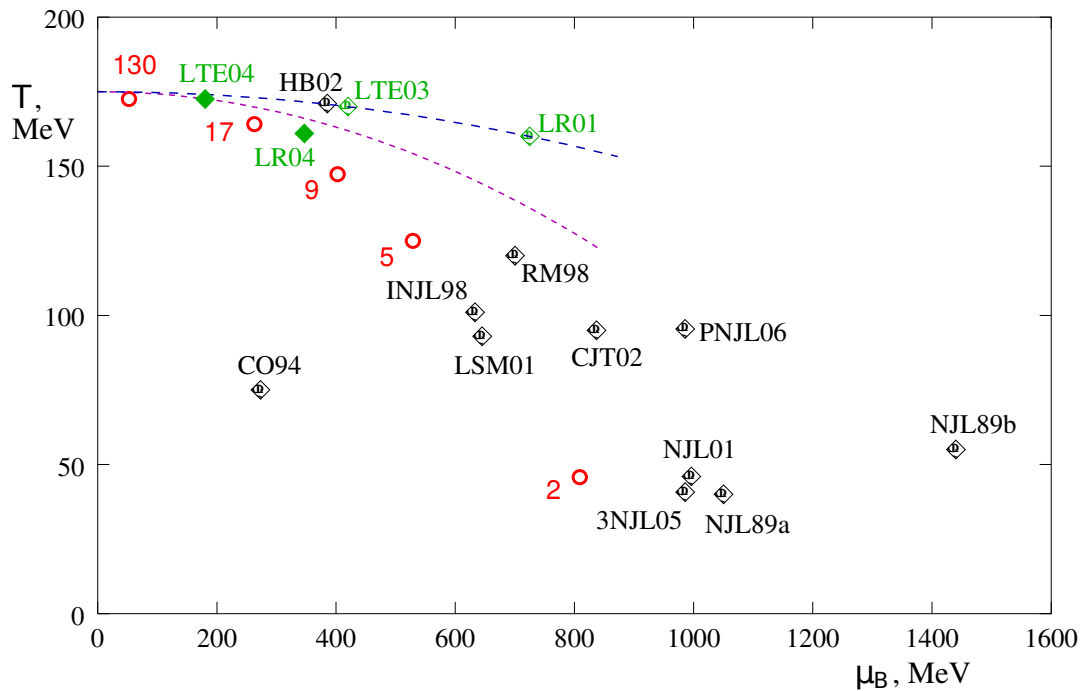
Figure 3: Comparison of predictions for the location of the QCD critical point on the phase diagram. Black points are model predictions: NJLa89, NJLb89, CO94, INJL98, RM98, LSM01, NJL01, HB02, CJT02, 3NJL05, PNJL06.
Green points are lattice predictions: LR01, LR04, LTE03, LTE04.
The two dashed lines are parabolas with slopes corresponding to lattice predictions of the slope $dT/d\mu_B^2$ of the transition line at $\mu_B = 0$.
The red circles are locations of the freezeout points for heavy ion collisions at corresponding center of mass energies per nucleon.
image and caption credit: [2]

3.5 Experimental approach – Heavy Ion Collisions

The available theoretical estimates suggest that the searched critical point is located in a temperature-density region available at heavy-ion collisions experiments. Colliding various
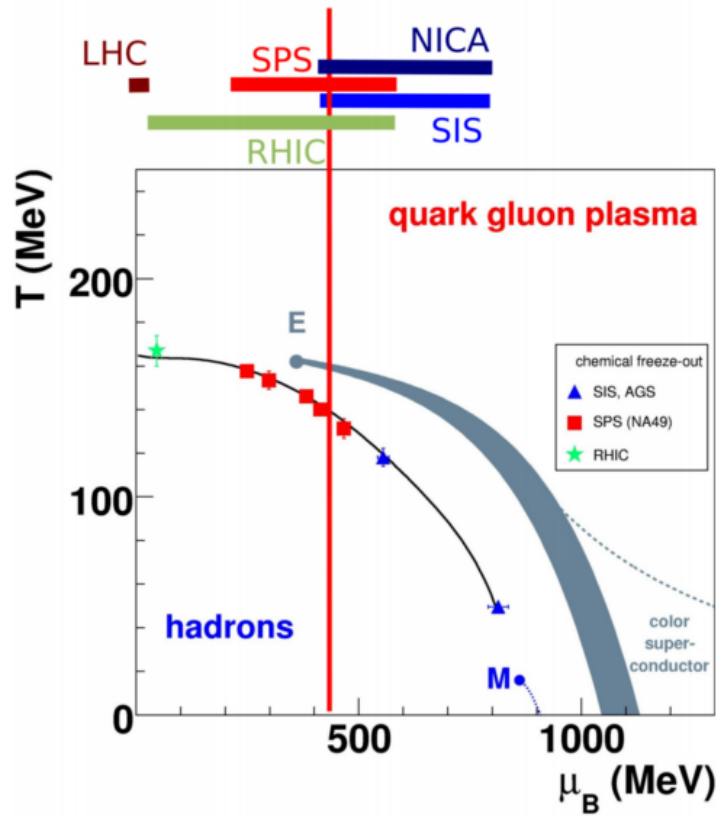
Figure 4: The world effort of studying a QCD phase diagram.
image credit: Marek Gaździcki

atoms at various energy allows allows to probe the phase diagram in both: T and μ_B directions.

The information about the location of the freeze-out point hides in the ratios of certain particle yields (e.g. baryons or antibaryons to pions). As for the critical point one needs to measure event-by-event fluctuations.

The search of phase transitions in QCD is, were or will be conducted by following experiments:

- **AGS at Brookhaven Natinal Laboratory (BNL)** – started operation in 1960 and now serves as the injector for RHIC.

- **STAR and PHENIX detectors at Relativistic Heavy Ion Collider**, which studies QGP formation at energies in range 4.9-50 AGeV, with an event rate of 1Hz. STAR began operation in year 2000 and PHENIX in 2011.

- **ALICE experiment at Large Hadron Collider (LHC at CERN)**, which studies QGP formation in Pb-Pb collisions at energies reaching 2.76 TeV. In operation since 2010.

- **NA61/SHINE at Super Proton Synchrotron (SPS at CERN)** – in operation

since 2011. The Pb beam energies are in range 4.9-17.3 AGeV, with an event rate at 100Hz.

- **MPD at The Nuclotron-based Ion Collider facility (NICA)** – due to start in a near future. Designed to study hadrons in dense matter, will operate below the energies of 9 AGeV, with an event rate up to 10kHz.

- **CBM experiment at SIS-300 facility in GSI** – planned to be built in a near future. Will operate on the energies allowing the study of hadrons in dense matter with extremely high event rates of 10Mhz

4 Physics goals of NA61/SHINE

4.1 Overview

NA61's comprehensive study has the following main objectives [7]:

- Search for the critical point by an energy – system size (E-A) scan.

- Study the properties of the onset of deconfinement by the E-A scan.

- Investigate hadron production in p+p and p+Pb collision as a reference for Pb+Pb data, with particular focus on correlations, fluctuations, and high transverse momenta.

- Obtain high precision data on hadron production in hadron-nucleus interactions for the T2K neutrino experiment and cosmic-ray experiments: Pierre Auger Observatory and KASKADE.

4.2 Onset of deconfinement

The very basis of the search for the onset of deconfinement and the critical point are predictions of the Statistical Model of the Early Stage [8]. The primary assumptions of the model are listed below:

- The phase transition between hadronic matter and QGP takes place at $\sqrt{S_{NN}} \approx 7\text{GeV}$.

- There exists a 1-st order phase transition in a whole μ_B range – consequence of using the Bag model equation of state.

- Existing phases of matter: confinement $\rightarrow$ mixed phase (at $T_C = 200\text{MeV}$) $\rightarrow$ deconfinement.

- Quarks and gluons at an early stage are in thermal equilibrium.

- The number of internal degrees of freedom increases in transition to QGP due to the activation of parton degrees of freedom.

- The entropy in a final stage is proportional to the total number of pions (main entropy carriers).

- The total number of created strange quarks and the total entropy are equal before and after hadronization. This way the entropy created in QGP cannot decrease while going back to hadron phase.

The SMSE gives both qualitative and quantitative predictions of pion and kaon production. There are three main characteristic features predicted by the model (see Fig.5):
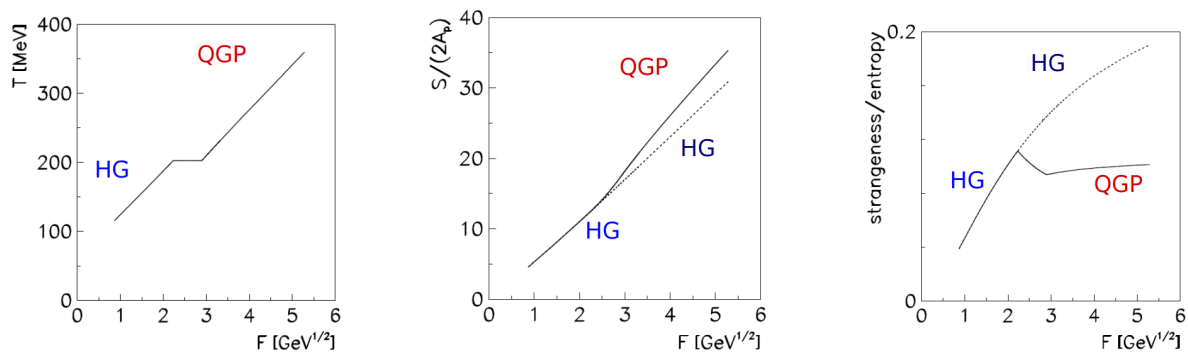
Figure 5: The theoretical prediction of anomalies in particle ratios according to SMSE: the step, the kink and the horn
image credit: Marek Gaździcki

The energy dependence is pictured in a Fermi variable frame:

$$F = \frac{(\sqrt{s_{NN}} - 2m_N)^{3/4}}{(\sqrt{s_{NN}})^{1/4}} \approx \sqrt[4]{s_{NN}}$$

The kink:

The total entropy to number of participating nucleons ratio ($S/2A_p$) as a function of energy (here: Fermi variable F) should increase linearly with an energy. The slope of this function should be proportional to $g^{1/4}$, where g is the number of internal degrees of freedom. The value of g is higher in a QGP phase, than it is in hadron gas, therefore we should observe a more steep slope where there is a creation of QGP.
As one can see in the Fig. 6 such prediction found an experimental confirmation.

The step:

The step structure is visible in a relation of the temperature (here: inverse slope parameter of transverse mass distribution T) and energy (here: Fermi variable F). According to hydro-dynamical approximation we expect the temperature to rise along with a energy density. On the other hand, in case of a mixed phase the temperature ought not to depend on energy. The SMES states that inside a mixed phase region we should expect a plateau in $T(F)$ function. The step was also observed in experimental data, as seen in Fig. 7.
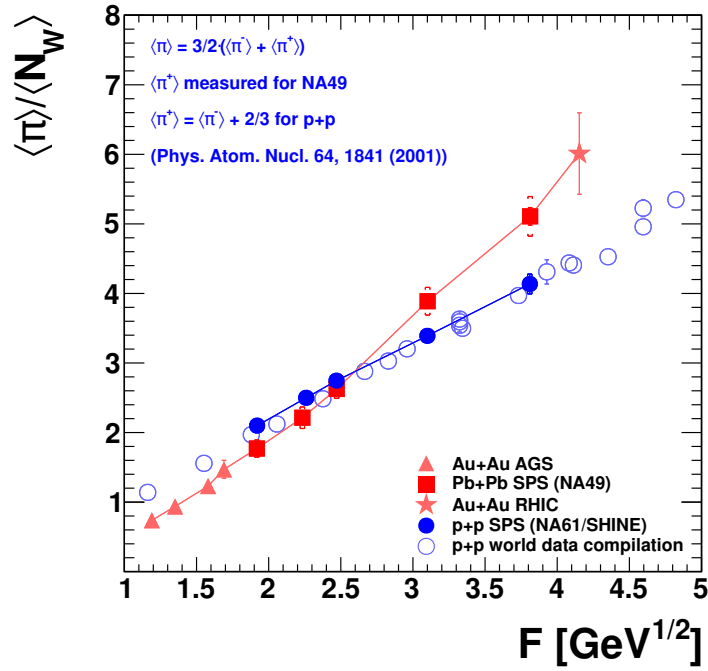
Figure 6: The experimental data confirming the SMSE prediction of a presence of the kink structure. It shows a pion multiplicity to the number of participating nucleons ratio. The pions are main entropy carries, therefore pion data is interpreted as an entropy information.
image credit: [9] and Szymon Puławski
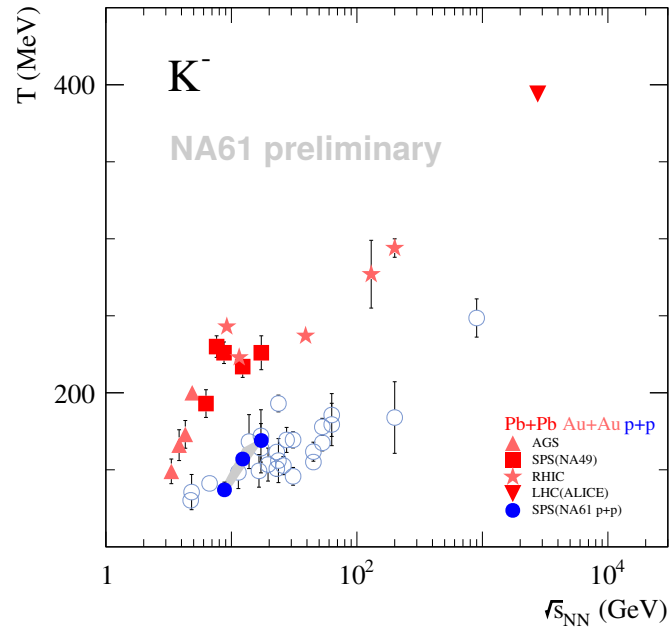
Figure 7: The experimental data confirming the SMSE prediction. It shows the inverse slope parameter of transverse mass distribution in a function of energy in a Fermi variable F.
image credit: [9] and Szymon Puławski

The horn:

The most spectacular structure of a peak in a vicinity of phase transition in a strangeness to entropy ratio in a function of an energy (again – variable F). For an ideal gas of massless particles the SMES predicts the strangeness to entropy ratio $\frac{1}{4} \cdot \frac{g_s}{g}$ (g_s – the number of strange degrees of freedom, g – total number of degrees of freedom). The transition from massless hadrons to massless quarks QGP causes decrease of strangeness to entropy ratio by a factor of 2. Setting a finite mass to quarks needs to take into account two additional problems: a change of total number of degrees of freedom and a reduction of mass of strangeness carriers in QGP ($m_{K,\Lambda} \to m_s$). Considering those we obtain finally a rapid increase of strangeness to entropy ratio for low energies, then a decrease of that ratio in a mixed phase down to the value expected in a QGP phase.

In the Fig. 8 the experimental data is plotted along with various model predictions.
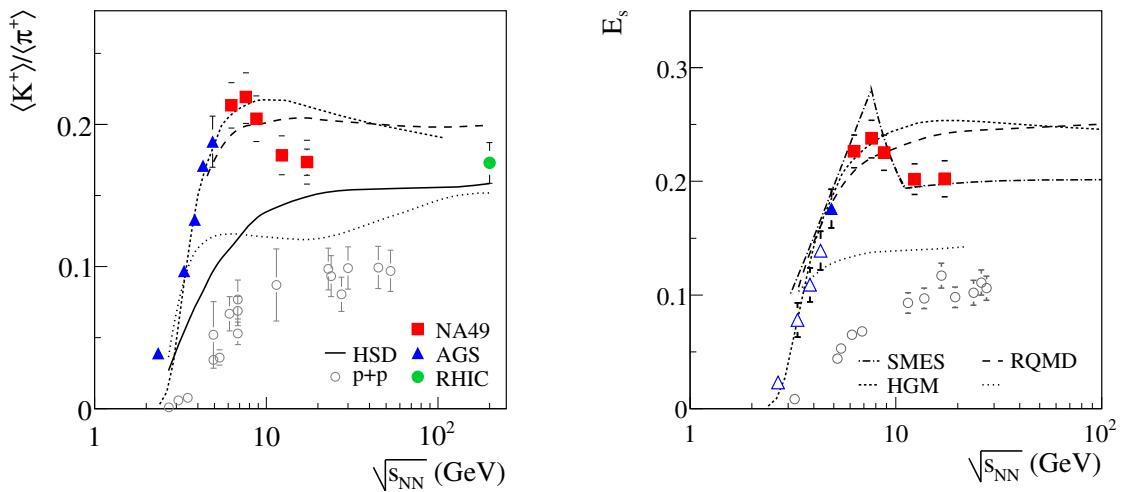
Figure 8: The experimental data confirming the most famous SMSE prediction.
Left: Energy dependence of the $\langle K^+ \rangle / \langle \pi^+ \rangle$ ratio measured in central Pb+Pb and Au+Au collisions (full symbols) compared to the corresponding results from $p + p(\bar{p})$ reactions (open circles).
Right: Energy dependence of the relative strangeness production as measured by the E_S ratio (see the equation #) in central Pb+Pb and Au+Au collisions (full symbols) compared to results from $p + p(\bar{p})$ reactions (open circles). The curves in the figures show predictions of various models, including SMSE.
image credit: [9]

4.3 Critical point

In order to find the critical point in the QCD phase diagram we need to gather a huge amount of experimental data, probing various point of the diagram. Varying the energy and the system size we search for the increase in event-by-event fluctuations of transverse momentum and multiplicities.
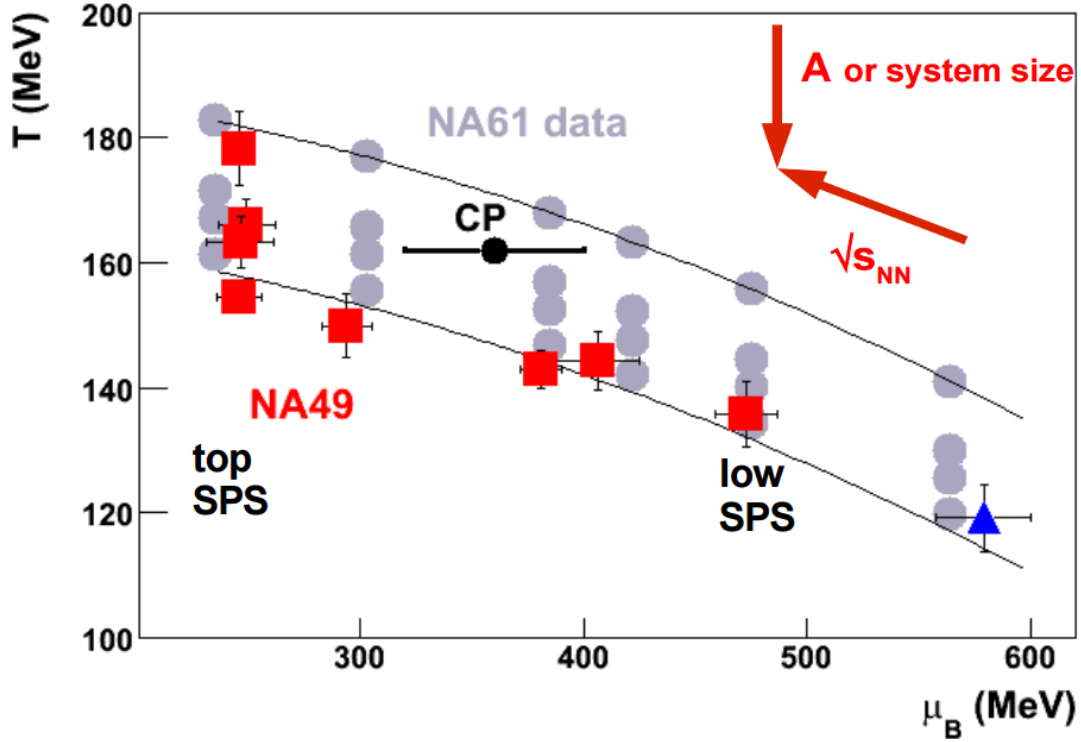
Figure 9: The QCD phase diagram with denoted probing points of the NA61/SHINE experiment.
image credit: Katarzyna Grebieszkow

To measure the fluctuations we use two variables:

Fluctuations in a transverse momentum: Φ_{p_T}

$$\Phi_{p_T} = \sqrt{\frac{\langle Z_{p_T}^2 \rangle}{\langle N \rangle}} - \sqrt{\overline{z_{p_T}^2}}$$

where $z_{p_T} = p_T - \bar{p_T}$ for a single particle and $Z_{p_T} = \sum_{i=1}^{N} \left(p_T^i - \bar{p_T} \right)$ is summed over particles participating in a collision.

Fluctuations of multiplicities:

$$\omega = \frac{\langle N^2 \rangle - \langle N \rangle^2}{\langle N \rangle}$$

The search for the critical point carries the most significant discovery potential for the NA61/SHINE experiment.

4.4 Neutrino physics

A quantum phenomenon of neutrino changing its lepton flavour periodically on its way through space, called neutrino oscillations, is at present one of the most challenging topics in particle

physics. Various experiments are carried out to study neutrino masses and mixings. High-precision measurements at T2K experiment provide us with an insight into the mixing mechanism.

The T2K experiment studies oscillations of a muon neutrino beam between the J-PARC accelerator and the Super-Kamiokande detector, 295km away from each other [10]. The main goal of T2K are:

- to determine parameters θ_{23} and Δ_{23}^2 by measuring the $\nu_\mu \to \nu_x$ disappearance,

- measurement of the unknown mixing angle θ_{13} by the observation of the $\nu_\mu \to \nu_e$ appearance signal,

- measurement of neutral current events with sensitivity more than an order of magnitude better than any previous measurements.

Where is the NA61/SHINE in all this? In the absence of a good theory of hadronic interactions, an extraordinary level of precision is required for a reliable prediction of the properties of such neutrino beams . The role of the NA61/SHINE experiment is to perform these hadron production measurements in the most sterling way. More specifically the experiment measures the production of charged pions and kaons out of a thin carbon (4% of a nuclear interaction length), as well as the full replica of the T2K target (a 90 cm graphite cylinder). This allows for precise calculations of the initial neutrino fluxes and beam composition at J-PARC, which leads to the best possible estimate of several neutrino properties, such as neutrino mixing angles.
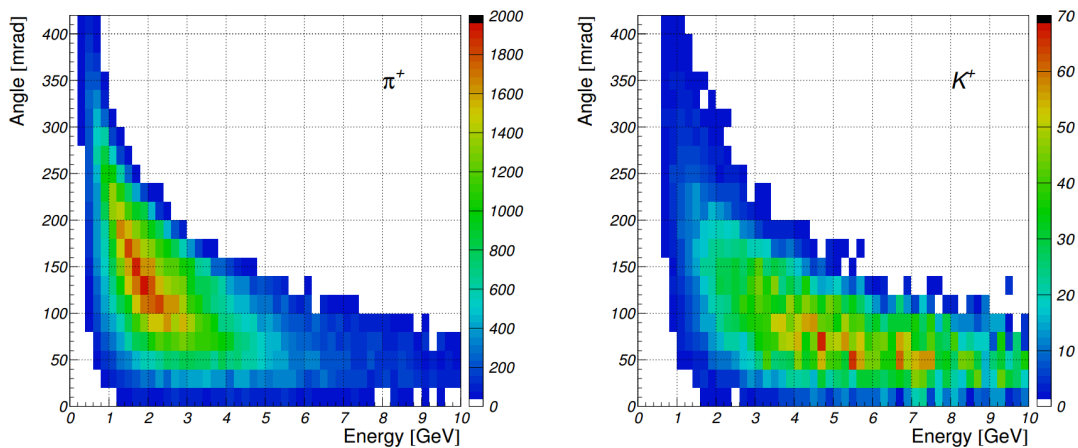
Figure 10: Momentum p vs. polar angles at the production point θ distribution of π^+ mesons (left) and K^+ mesons (right) that contribute to the neutrino flux in the T2K detectors.
image credit: KASKADE

4.5   Cosmic ray physics

Despite of discovery of cosmic rays as long ago as in 1912, our knowledge of cosmic rays is still vastly limited. The unknown properties remain: source and propagation, but also the spectrum

and the composition at high energies. Knowing how the elemental composition of cosmic rays depend on the energy is essential to explaining phenomenons such as 'the knee' at 3×10^6 GeV (change of the power-law index of the cosmic ray flux) or the transition from galactic to extra-galactic rays around 10^9 GeV. Knowledge about a composition of mentioned cosmic rays is essential for confirming or ruling out various ultra-high energy cosmic ray models, many of which postulate an onset of new physics.
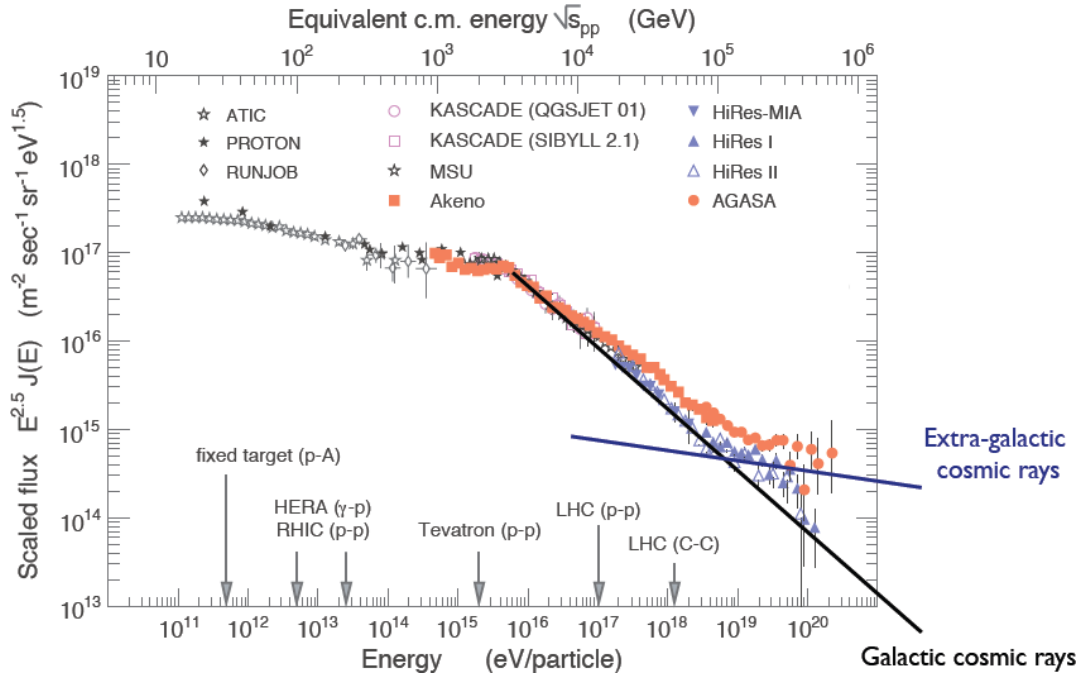
Figure 11: The knee and the transition from domination of galactic to extra-galactic cosmic rays at energies of 3×10^6 GeV and 10^9 GeV accordingly.
image credit: Marek Gaździcki

Above the energy of 10^5 GeV the particle flux is so low, that instead of direct particle detection there is a necessity to analyze secondary particle showers produced in the interaction with the atmosphere (called *extensive air showers*). Therefore in order to obtain the rays' properties with a good reliability we need a detailed modeling of the various interactions and decays of the shower particles.

The high-precision experiments as KASKADE and Pierre Auger Observatory are measuring several observables of each cosmic ray shower. The most significant contribution to final results' uncertainties arises from predicting the hadronic multi-particle production. Unfortunately such predictions are still not in the range of QCD calculations, therefore modeling of cosmic-ray interactions depends vitally on the accelerator experiments measurements. This allows tuning of existing phenomenological particle production models.

5 Experimental setup

The NA61/SHINE experiment origins date back to the year 2006, when the proposal was submitted to CERN SPS Experiments Committee [7]. The first physics data with hadron beams was recorded in 2009 and with ions in 2011. The NA61 experiment inherited most of the detector components from its predecessor – NA49 and in fact continues its mission of investigating the quark-gluon plasma.

The experiment operates on Super Proton Synchrotron beams of extremely wide energy range – form just over 10 GeV/c up to almost 400 GeV/c.

5.1 Acceleration chain
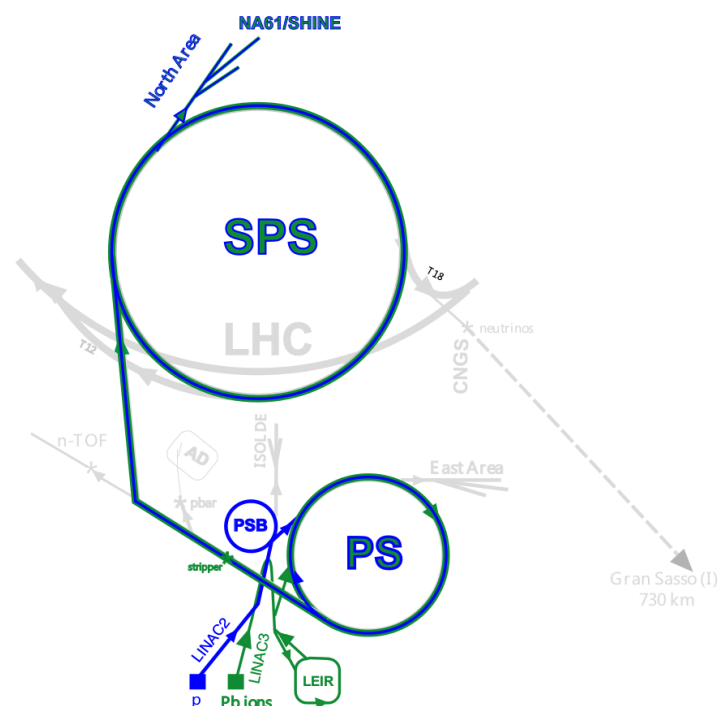
Figure 12: Schematic layout of the SPS acceleration chain relevant for the NA61/SHINE experiment. *image credit: [11]*

NA61/SHINE uses beams of three main categories: proton, ion and hadron beams. For each of them there is a necessity for a different acceleration chain:

Proton Beams:

1. The starting point is the hydrogen gas.

2. The Radio-Frequency Quadrupole RFQ2 focuses and bunches the beam. Accelerates it to 750 keV.

3. Protons are injected into three-tank Alvarez drift tube LINAC2 with a total length of

33.3 m. The final energy the beam reaches here is 50 MeV. Such an energy corresponds to one-third velocity of the light.

4. The four rings of Proton Synchrotron Booster (PSB) add the acceleration of two orders of magnitude with resulting beam energy of 1.4 GeV.

5. Now protons are extracted to Proton Synchrotron, CERN's oldest accelerator. With a circumference of 628 m, it is capable of accelerating the protons to 14 GeV/c (momentum). At this point the velocity of the particles is as close to the speed of light as: 0.999 c.

6. The final stage of the acceleration is performed by the Super Proton Synchrotron. The top SPS proton beam momentum is 400 GeV/c.

Ion (lead) Beams:

1. Here a starting point is an isotopically pure ^{208}Pb, which is inserted into the ECR source crucible. The ions extracted from the source carry the energy of 2.5 keV/u.

2. The $135°$ spectrometer selects the ions of Pb^{29+}.

3. The RFQ and then the RF cavity in the LINAC3 accelerator give a boost to the 4.2 MeV/u.

4. Now the ions go through the first stripping stage – 0.3μm carbon foil, which is followed by another spectrometer, choosing Pb^{54+} ions for a further acceleration.

5. The beam enters Low Energy Ion Ring and reaches the energy of 72 MeV/u. At this point the total beam intensity is about 10^9 ions.

6. Next acceleration step is the injection into the Proton Synchrotron. At the exit of the PS, the beam traverses the final stripping stage, producing Pb^{82+} with the energy of 5.9 GeV/u.

7. The two bunches, $3 \cdot 10^8$ ions each are now injected into the SPS, where they reach the final energy in the range between 13 GeV/u and 160 GeV/u. Both boundaries are due to the construction of the accelerator.

Hadron Beams:

Hadron beams for NA61/SHINE are produced at the T2 target, located in the North Area target cavern, about 1 km from the SPS extraction spot. The T2 target station hosts several beryllium plates of different lengths. The hadrons are produced from the impact of the primary proton beam from the SPS and as the secondary beam particles are transported to NA61/SHINE production target, 535 m away.

The provided hadron beams are in the momentum range of 13 GeV/c to 158 GeV/c, with a typical momentum spread lower than 1%.
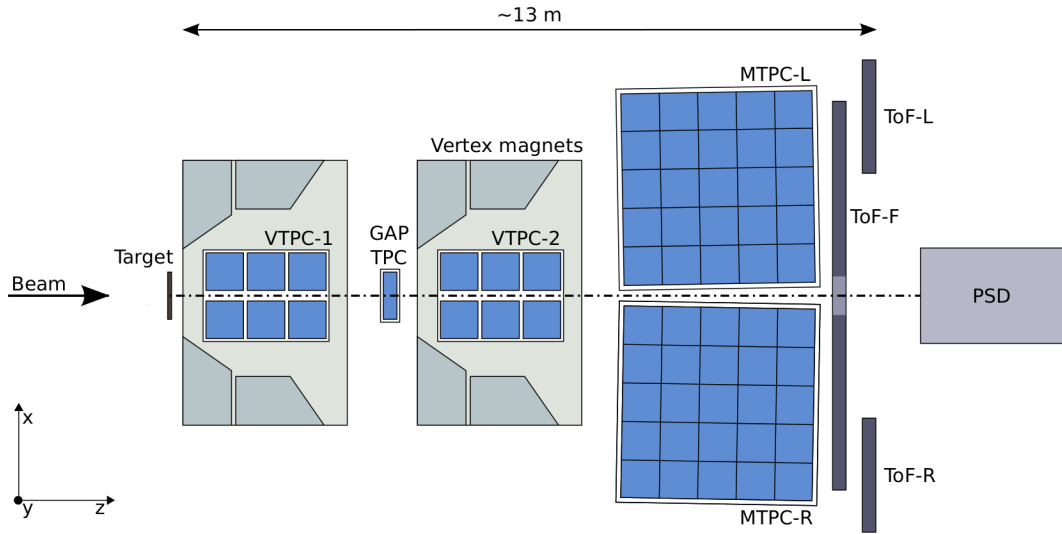
5.2   Particle Detectors Overview

Figure 13: The layout of the detectors in the NA61/SHINE experiment. The beam is entering the set from the left side of the picture, along the z-axis.

The information used in this paragraph was taken from the NA61/SHINE facility paper – [11]

Beam Counters

The first encounter upstream of the target, is the set of scintillators, beam position detectors and Cherenkov counters (none of them denoted in the picture). Scintillators provide us with a precise time reference information, which later on is used for time-of-flight calculation, crucial for low-multiplicity events. BPDs on the other hand are delivering the position of the beam particles, on the plane perpendicular to the beam, with a precision of $\approx 100\mu m$. From this information the straight line trajectory is derived. Another measured observable is the particle charge from the Cherenkov counters. Described beam counters account altogether for precise trigger settings.

Time Projection Chambers

Downstream of the target there are five Time Projection Chambers. Two of them – Vertex TPCs – are placed in the field of super-conducting dipole magnets. Between VTPCs there is the Gap TPC and further, there are two biggest chambers – Main TPCs. Detailed description of drift chambers will be provided in a following section.

Time-of-Flight Detectors

Next on the beam line there are Time-of-Flight detectors. The addition of the ToF systems allows us to identify particles correctly in the neuralgic crossover region of the Bethe-Bloch curves. Detectors on sides – ToF-Left and ToF-Right – were inherited from the NA49 experiment, while the ToF-Forward was added by NA61 to satisfy the demand of the extended

particle identification for neutrino physics needs. ToFs right and left, combining for 4.4 m^2 total surface, consist of 891 rectangular scintillators each. They are 23mm thick and 34mm high, while their horizontal dimension vary: 60, 70 or 80mm. Each plate is coupled to a single photomultiplier. The Tof-Forward consists of 80 scintillators – oblong rectangles oriented vertically, totalling for 720×120 cm^2 active area.

The time resolution of those incredibly accurate stopwatches is said to be (p+p and Be+Be collisions): 80 ps for ToF-R, 95 ps for ToF-L and 110 ps for ToF-F. Such accuracy allows for distinction of pions and kaons with momentum up to 5 GeV/c (when used along with dE/dx information).

Projectile Spectator Detector

The installation of the forward hadron calorimeter was one of the most crucial NA61 upgrades in the inherited experimental setup. The purpose of the PSD is to measure the total energy of the projectiles in nucleus-nucleus collisions. Its event-by-event energy measurements are precise enough to enabling the extraction of the number of nuclei participating in the collisions with a precision of one nucleon. Such high energy resolution is also important for the study of possible fluctuations in hadron production properties, which we expect to observe in the transition region between the hadronic matter and the quark-gluon plasma.

The design of the calorimeter is briefly denoted in the image below. The basic principle of operation lays in the alternately placed layers of lead and scintillators. The lead layers decelerate incoming particles and the scintillators provide an information of passing particles.
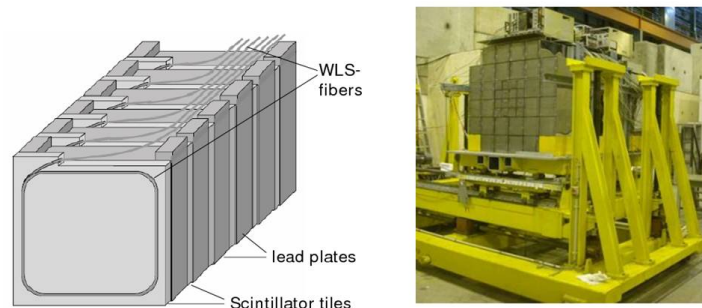
Figure 14: The design of each module of Projectile Spectator Detector (left) and the photograph of the calorimeter in the experiment area (right).

5.3   Time Projection Chambers

The main tracking devices in the NA61/SHINE experiment are Time Projection Chambers. The chamber consists of a large gas volume, in which particles leave ionized trails. The volume is surrounded by a cage made of aluminized Mylar strips, which voltages are tuned by a divider chain in order to obtain an electric field as close to uniform as possible.

Figure 15: The outside view on one of the Vertex TPCs. Mylar strips are visible surrounding each side of the cage.

5.3.1   Principle of operation

In a quasi-uniform electrical field the electrons from primary ionization drift with a constant velocity towards positive values of y-axis and towards the top plate, where their position, arrival time and total number are measured. The top plate is subdivided into tiny pads, which are responsible for converting the arriving electron cloud into the electronic signal and this way provide us with an information about z-axis and x-axis coordinates. The y-position is derived from the time of arrival of the electrons from the primary ionization. For a single particle track we obtain up to 160 measured points along the trajectory. From those data points the actual particle tracks are reconstructed and used for a further study. Together with up to 234 clusters and samples of energy loss we are provided with high statistic for precise measurements and finally a particle identification.

For purposes of this thesis it is useful to adduce a following array, containing detailed information about each of the TPCs with a special attention to the pad arrangement and the geometry.
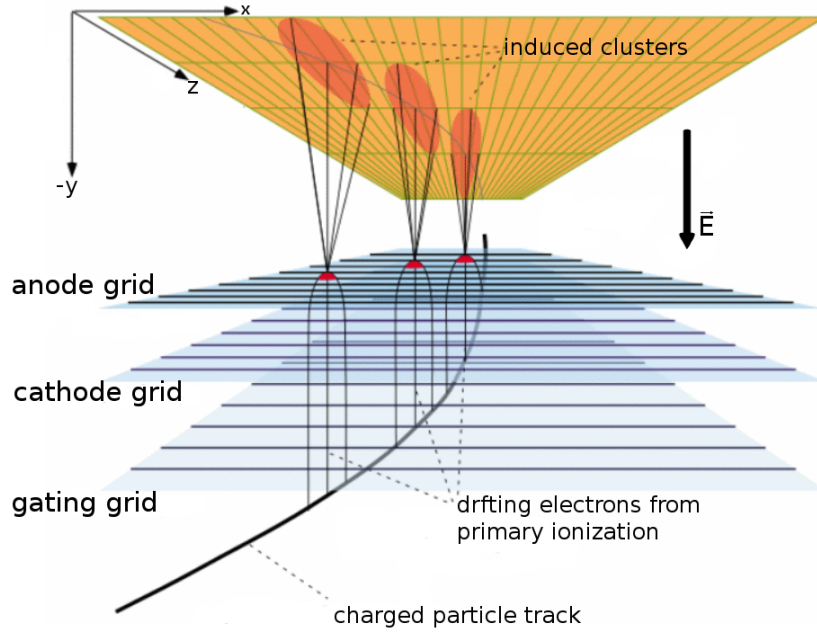
Figure 16: The principle of operation of the TPC. A charged particle wades through the gas, leaving an ionized trail. The electrons from primary ionization are drifted along the electrical field, towards the pad plain on the top.

	VTPC-1	VTPC-2	MTPC-L/R	GAP-TPC
size (L×W×H) [cm]	250×200×98	250×200×98	390×390×180	30×81.5×70
No. of pads/TPC	26 886	27 648	63 360	672
Pad size [mm]	3.5×28(16)	3.5×28	3.6×40, 5.5×40	4×28
Drift length [cm]	66.60	66.60	11.74	58.97
Drift velocity [cm/μs]	1.4	1.4	2.3	1.3
Drift field [V/cm]	195	195	170	173
Drift voltage [kV]	13	13	19	10.2
gas mixture	Ar/CO_2 (90/10)	Ar/CO_2 (90/10)	Ar/CO_2 (95/5)	Ar/CO_2 (90/10)
# of sectors	2×3	2×3	5×5	1
# of padrows	72	72	90	7
# of pads/padrow	192	192	192, 128	96
Readout surface	10m^2	10m^2	15.21m^2	0.25m^2
# of data points	72	72	90	<5

Table 1: In VTPC1 in the two upstream sectors there are narrower (16mm) pads in order to obtain better precision. Also five sectors of MTPCs, closest to the beam, consists of narrower pads and larger amount of them. The number of pads in all TPCs totals for about 180000.

The electrons that are drifted from the primary ionization carry a relatively small amount of energy – insufficient for inducing clear electronic signal. In order to amplify the electron cloud charge there is a three-layer wiring grid just above the pad plane. The first layer encountered

by the electrons is a **gating grid**, which operates in two modes: open or closed. Open gate wire plane lets the electrons go through, while in the closed mode each wire is set with alternately opposite sign voltage of 90V. This way electrons end up attracted to +90V wires, where being captured are not causing any further ionization and therefore no signal is being induced. As you can see in the plots below, gating grid, when closed, also prevents the ions from escaping into the active volume. The middle wiring layer is a **cathode grid**. Each wire is of the same positive low voltage, which does not stop the electrons, but rather directs them onto the next layer – **the anode grid**. The anode draws the electrons with a high positive voltage of +1550V. Accelerated electrons are captured by anode wires causing an ion shower, which is then repelled by a positive wires' voltage and directed straight onto pads. The pads collect the charge from the particle shower. In most cases one primary ionization hit causes the projection on the cluster of few (more than just one) pads.
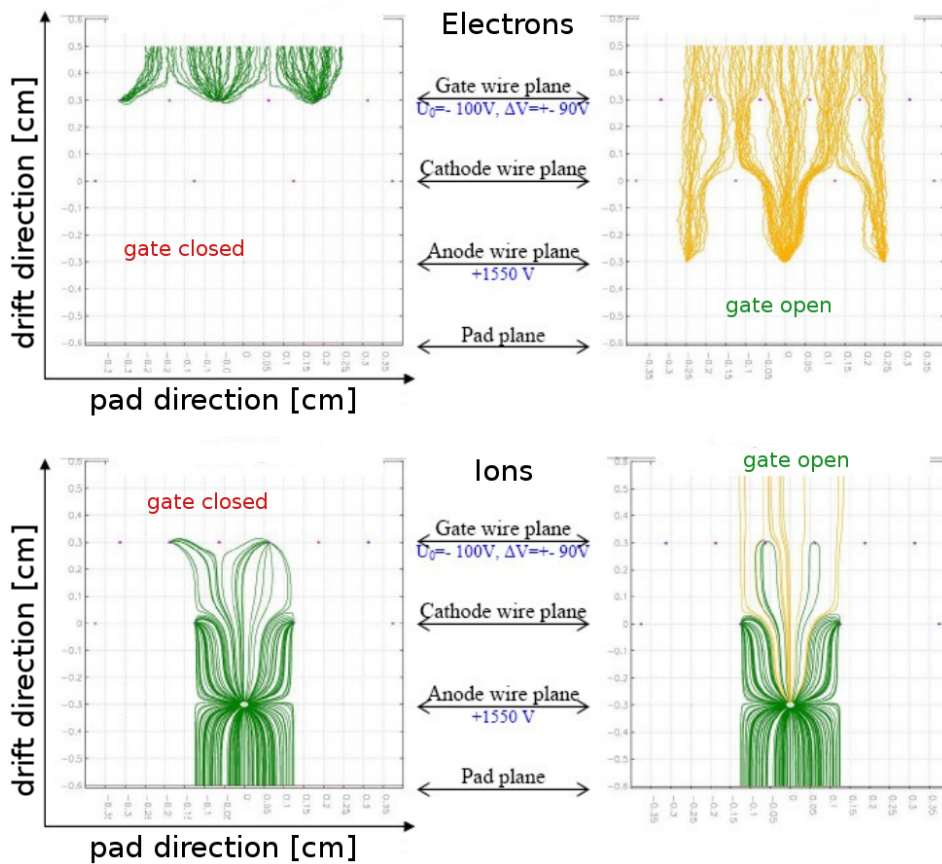

Figure 17: The image shows the simulated particle tracks in the region just below the pad plane of the TPC (for convenience it is pictured upside-down). Two upper plots show the tracks of electrons, while the lower plots show ions. The green colour indicates that particles have not crossed the gating grid and the yellow colour denotes overpassing ones.

5.3.2   Signal digitization

The total number of pads in all TPCs is exactly 182784, reading the signals from a total volume of 40m^3. This gives the largest contribution to the raw data of all subdetectors in the NA61/SHINE spectrometer. The readout of such a big data is quite an elaborate conception, which I will briefly introduce using the chart below.
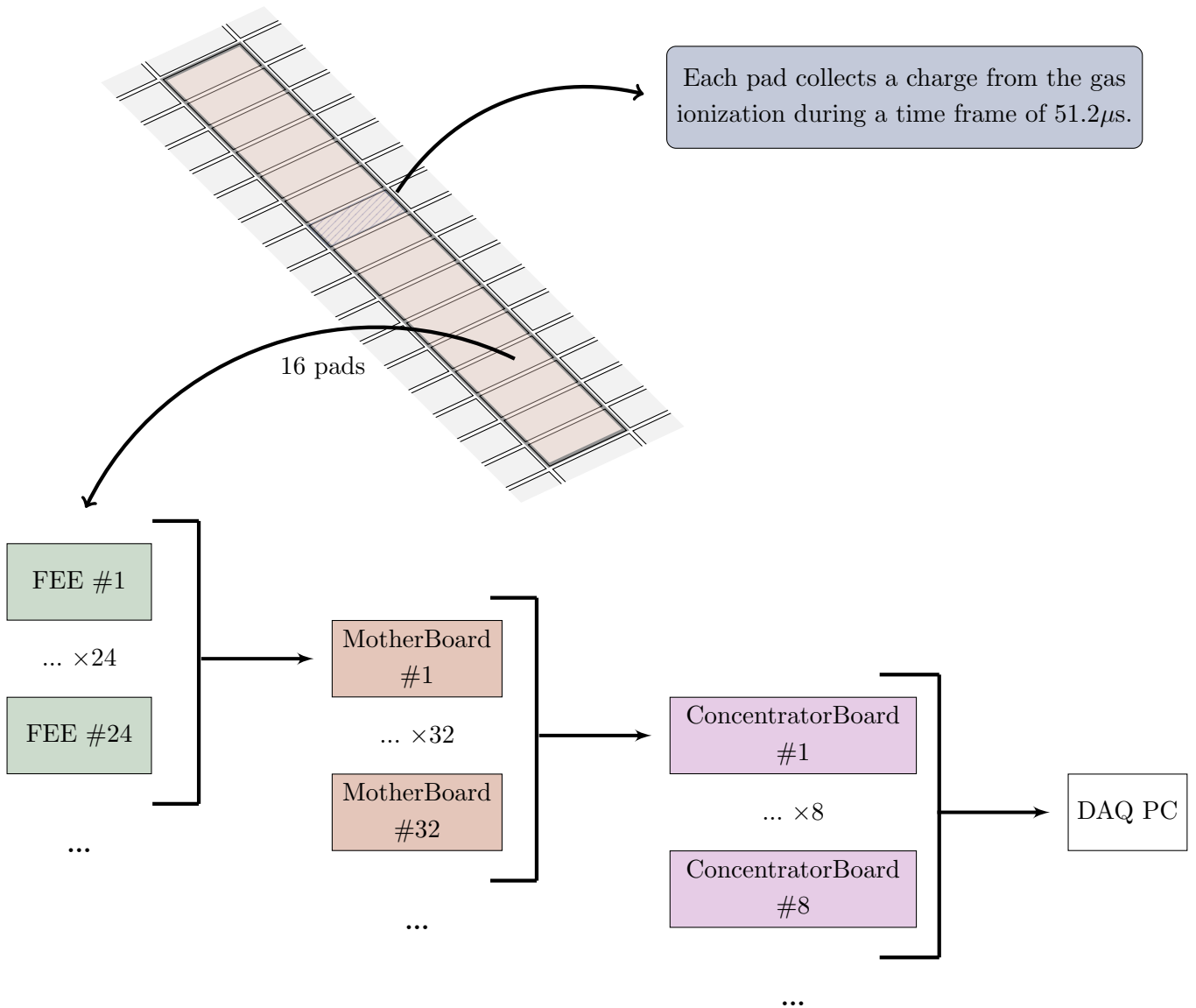
During a single event in the TPC, each pad collects a charge from drifted electron clouds in the time frame of 51.2μs binned in 256 or 512 samples. The first mode is used during the data acquisition due to the minimization of the data volume and the second mode is used for calibration runs.

Pad charges are transmitted in an analogue form to Front-End Electronics cards, where the signal is being preamplified and shaped using Switched Capacitor Array (SCA), then it is

digitized using a 9bit Wilkinson Analogue-Digital converter. One FEE is built up of two equal halves, each handling 16 pads. The FEE output is in the form of 1 Byte ADC values (Analogue to Digital Conversion).

MotherBoards read the digital signal from 24 FEEs simultaneously and following compression operations are performed:

- pedestal subtraction – the relative zero-level is calculated and deducted from all time slices,

- noise suppression – ADC values lower than 6 ADC ($\approx 2\sigma$ of the noise level) are substituted by a zero value,

- zero compression – an amount of consecutive zeros in the data stream is written as a single zero and the number of repetition.

The data streams are gathered by 8 ConcentratorBoxes and sent to the Data Acquisition computer. The snapshot of a single-event data in the final stage is pictured below.
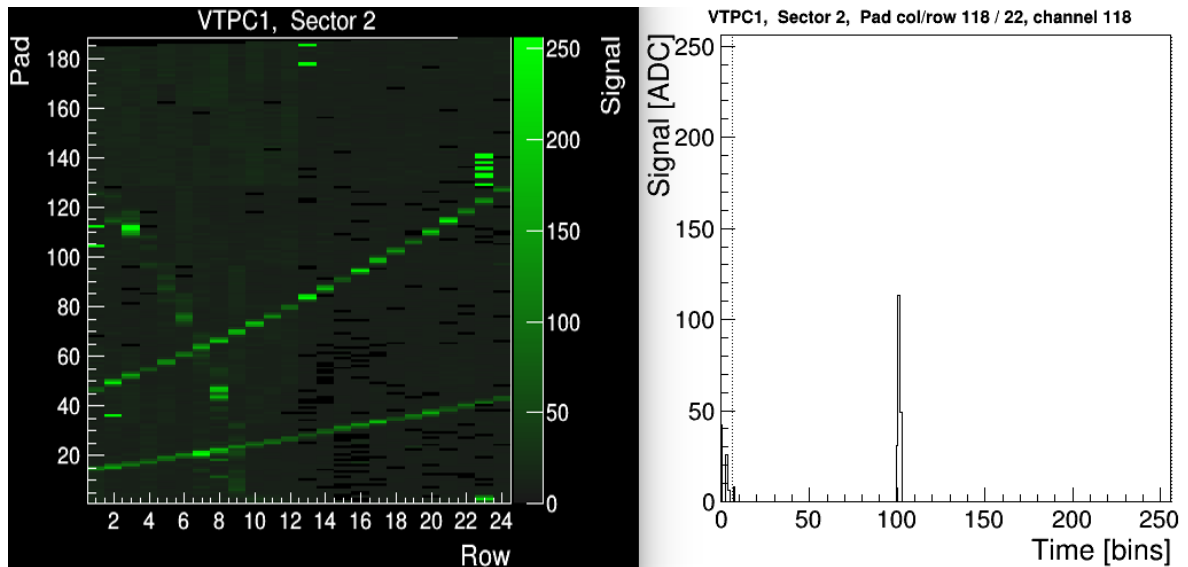
Figure 18: Left: Total charge collected by pads in sector 2 of VTPC-1. Fragments of particle tracks are clearly visible.
Right: A plot for a specific pad of the charge gathered in 256 time-slices in a $51.2\mu s$ time frame. Around 100-th time-slice the electron cloud from primary ionization reached the pad plane.

5.3.3   Detector performance

TPCs construction enables precise measurements of charge, momentum and mass of each charged particle. The final output data from the chambers is a set of over 100 points, where the ionization hits were recorded. TPCs mostly rely on measured energy loss, which is proportional to the total charge recorded by pads. Combined with the track curvature we are capable of calculating particle's properties listed above.

To show the physics performance reached by the chambers system I will present a study of the quality of measurements on the example of mass reconstruction of K_S^0 particles from their V^0 decay topology. Two p+p collision were analyzed at energies: 20 and 158 GeV/c. Measured peak positions are: 496.8±0.6 and 498.3±0.1 MeV/c^2. Those values agree reasonably with the PDG value of $m_{K_S^0} = 497.6$ MeV/c^2.
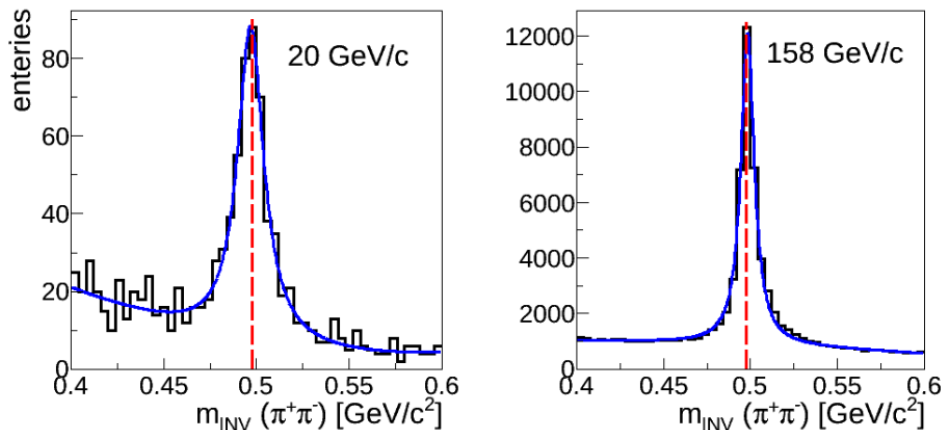

Figure 19: Invariant mass distribution of reconstructed K_S^0 candidates at 20 and 158 GeV/c. Fitted peak positions are: 496.8±0.6 and 498.3±0.1 MeV/c^2 and red dashed line shows the PDG value: $m_{K_S^0} = 497.6$ MeV/c^2.
image credit: [11]

The track reconstruction efficiency of negatively charged pions produced in p+p interactions at both energies does not fall below the 98% in the region of rapidity in range 0.0 to 3.0 and transverse momentum in range 0.0 to 1.5 GeV/c. The resolution of rapidity and transverse momentum for the same p+p collisions is pictured in the Fig. 20.

For the specific energy loss in the TPCs measured for p+p collisions @ 80GeV/c see the Fig. 22 in the next section.

6 Data analysis

6.1 Particle Identification

In order to identify a particle, the measurement of its mass is needed. For relativistic velocities we have a following formula bonding mass, momentum and velocity:

$$p = \gamma m_0 \beta c$$

To obtain the particle's mass we need to determine two of the observables present in the equation above: momentum p and velocity parameter – either γ or β (one can derive one from another). NA61/SHINE experimental setup allows to perform particle identification using three main methods described below.
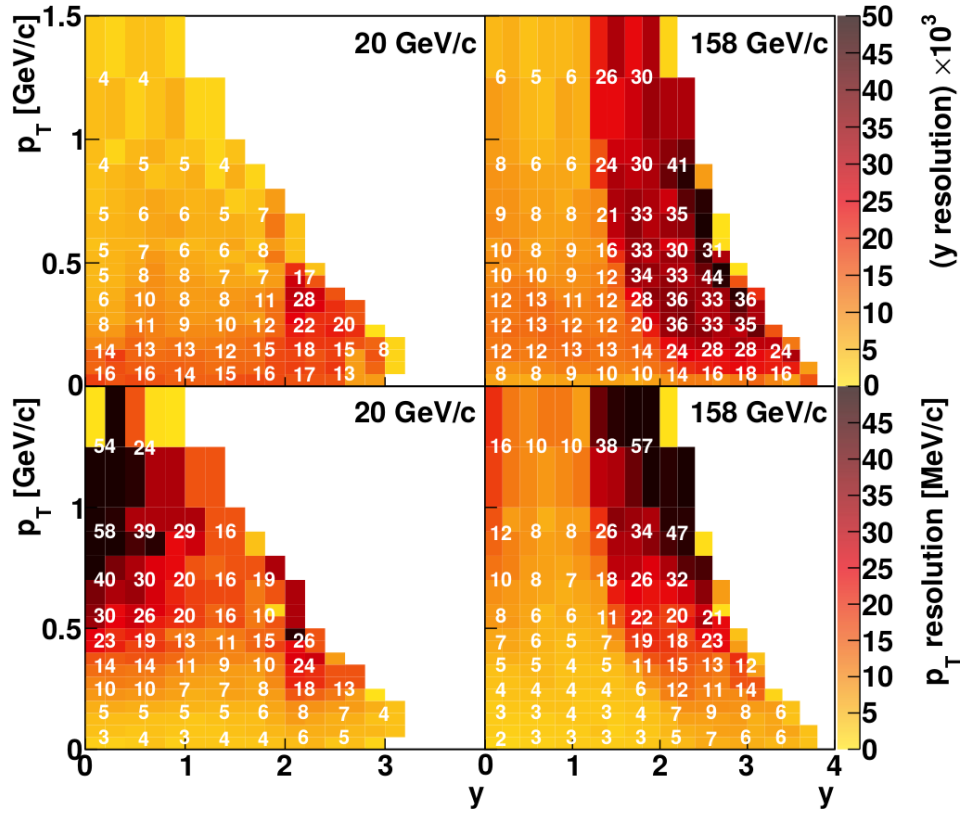
Figure 20: Top: resolution of reconstruction of rapidity ($\times 10^3$) in p+p interaction @ 20 and 158 GeV/c.
Bottom: transverse momentum resolution, also in p+p interaction @ 20 and 158 GeV/c.
(both values plotted as functions of rapidity and transverse momentum)
image credit: [11]
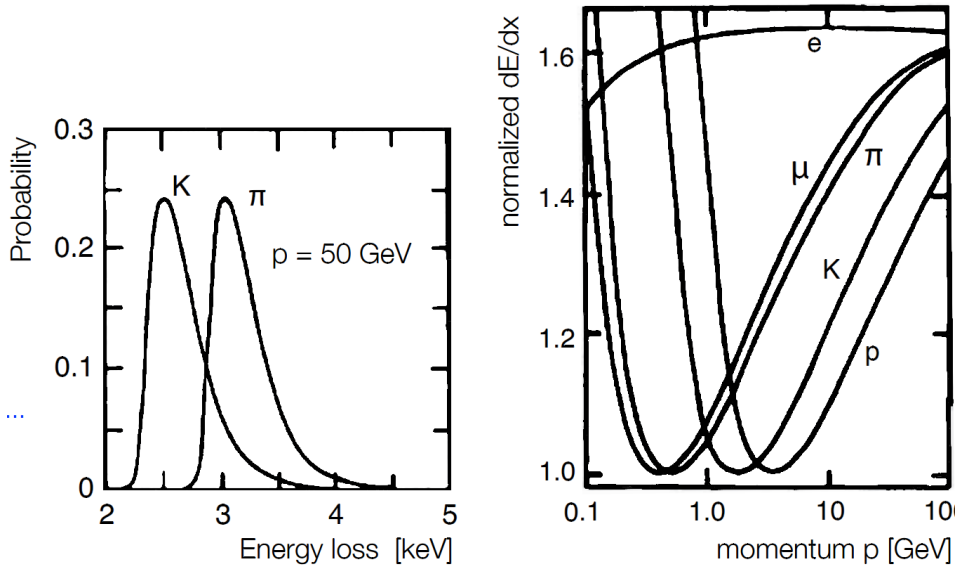
Figure 21: Left: theoretical dependence of the probability of the energy loss for two different particles going with a momentum of 50 GeV through the medium.
Right: Normalized energy loss versus particle momentum for various particles.

Energy loss (Bethe-Bloch curves)

Bethe-Bloch formula gives us following relation of energy loss of the momentum for a particle wading through the medium:

$$\frac{dE}{dx} \propto \frac{1}{\beta^2}\ln(\beta^2\gamma^2)$$

In the Fig. 21 the theoretical dependence is pictured and the real data is plotted in the Fig. 22.
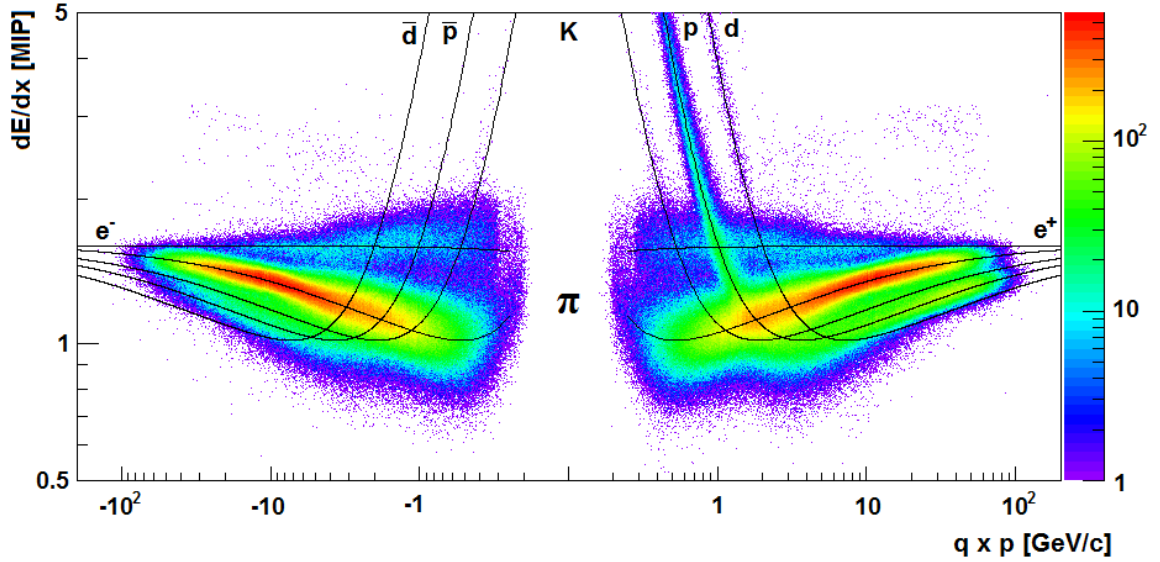
Figure 22: Specific energy loss, as measured in the TPCs for charged particles, pictured as a function of momentum. Data gathered in p+p collisions at 80 GeV/c. Solid curves show theoretical parametrization of the mean dE/dx for various particles.

Time of flight

We have a pretty straightforward relation linking the time of flight with the velocity: $\tau \propto 1/\beta$. In order to obtain a mass we need an external information about the particle's momentum. Then the relation is as follows:

$$m_0^2 = p^2\left(\frac{c^2\tau}{L^2} - 1\right)$$

With L being the distance of the flight.

Total energy

By measuring particle's total energy we can derive its mass from the simple relation:

$$E = \gamma m_0 c^2$$

6.2   Basic steps of NA61 analysis

6.2.1   Data structure

All the data of recorded events in NA61 spectrometer are saved in structures schematically pictured below.
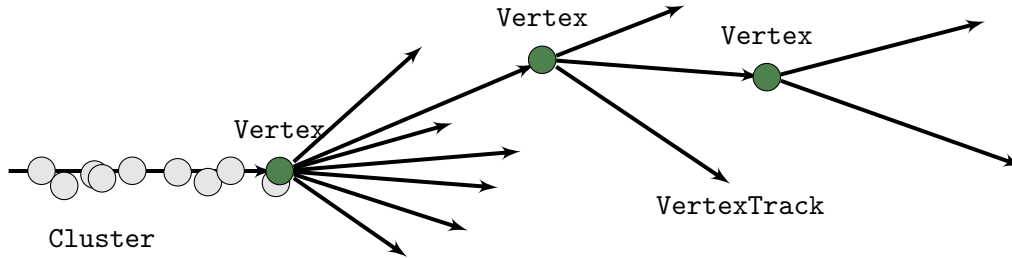
At first all the clusters (`Cluster`) in collected event are found. Then the clusters are grouped into tracks (`VertexTracks`), which are then attached to located decay points (`Vertex`). We obtain a structure, called Shine Offline Event – SHOE.

6.3   Data processing

The first operation on the SHOE file is the event selection, followed by a track selection for specific particles. The distributions of uncorrected data are saved, on which Monte Carlo based corrections are applied. Finally the distribution of corrected data, along with statistical and systematical errors is saved as a final experimental results.

Following the analysis chain, now the particle identification takes place. We are able to deduce particle **charge** q and its **mass** m. That is all the information we can get for short-lived hadrons:
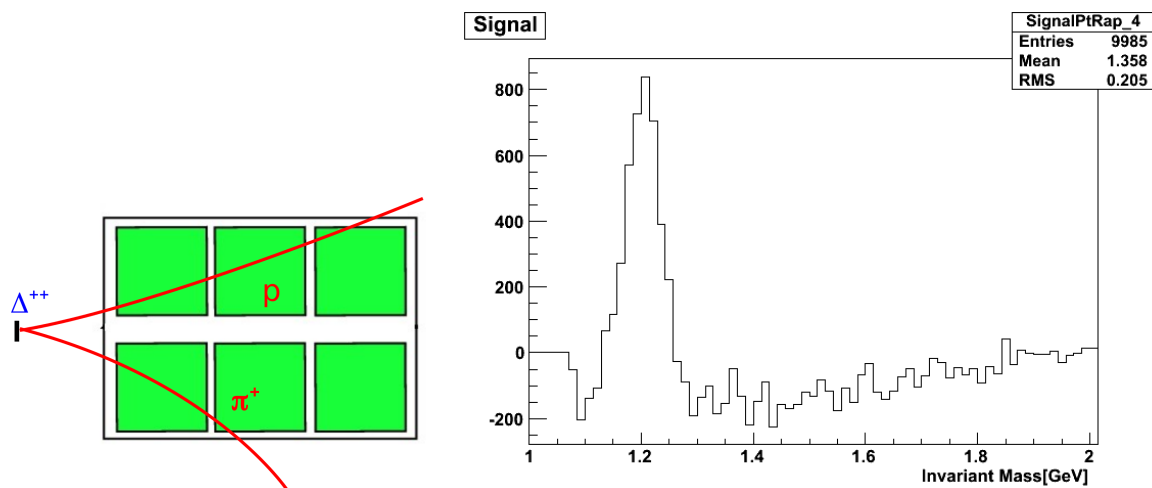
Figure 23: A short living hadron Δ^{++} ($\tau = 5.0 \cdot 10^{-24}s$) invariant mass and decay topology reduced to the production inside the target.

For the long living particles we are able to record also the description of its decay topologies.
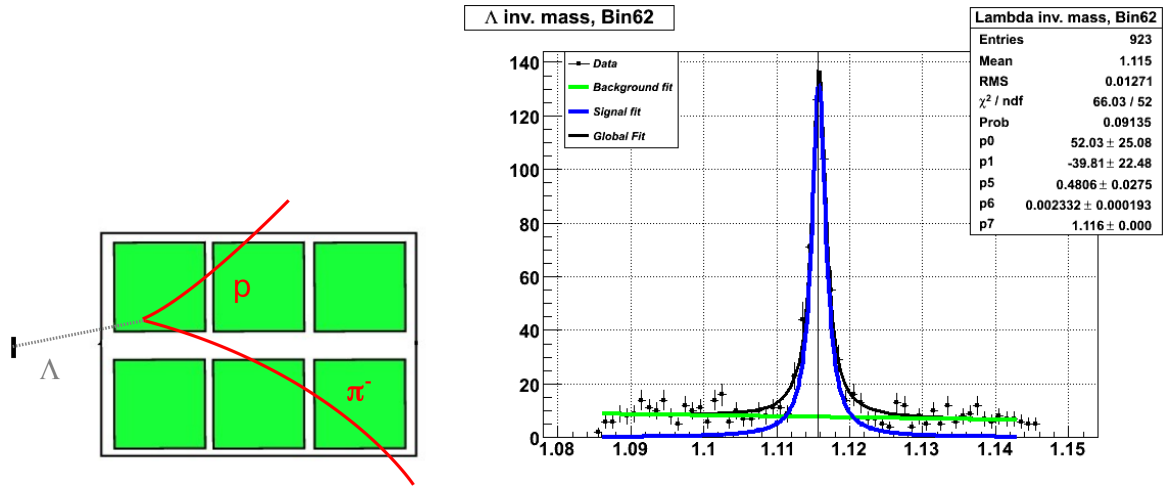
Figure 24: A long living hadron Λ ($\tau = 2.6 \cdot 10^{-10}s$) invariant mass and decay topology.

Part II

Method

7   Calibration procedure

7.1   Time delay t_0 calibration

The main goal of the calibration procedure is to reduce the error from the time measurement of particles arriving from the primary ionization. Being specific we aim to tune the 180 thousands of tiny stopwatches (TPC pads) with as high precision as there can be achieved.

Time shifts between the pads are distinguished into two categories:

- **Chip-to-chip**

  Those are relatively large variations of the time delay. They occur due to trigger cable length variations. 16 pads are connected to one chip, so we observe a significant t_0 delay difference in those exact intervals (see: fig. **??**).

- **Pad-to-pad**

  Pad-to-pad t_0 variations are at least an order of magnitude smaller, caused by a signal shaping time differences.
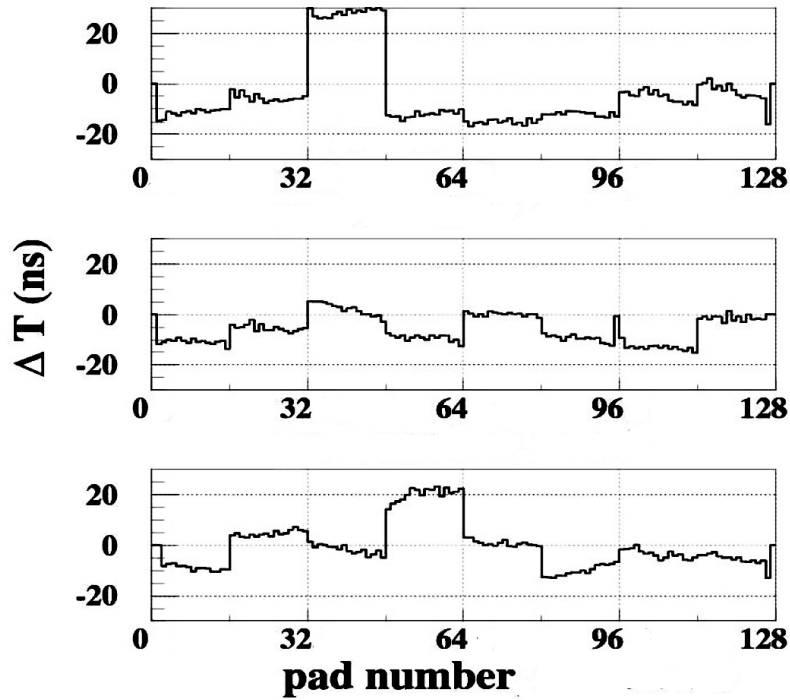
Figure 25: Time delays t_0, as recorded in MTPCL, sector 2.
image credit: Reiner Renfordt

7.2   Gain calibration

Secondary goal of the calibration is measuring the electronic gain of each pad. The variations of this value among pads are significant (up to 100%). They are a crucial factor for a detector performance, since the total charge collected by each pad is a source of the information on particle energy loss (see: section 6.1).

7.3   Pulser tool

Pulser is a hardware system attached to a wiring grid over the pad plane in TPCs. It is connected to the cathode wires, where it may apply a certain voltage. For the purpose of the calibration we inject a charge onto the cathode grid, revoking a step-like change of voltage. A new electric field causes a charge dislocation in pads, resulting with a signal peak. In the ideal world, the ideal step function would cause an ideal Dirac's delta response function. In this case the step is not perfectly steep and we are dealing with massive charge carriers, so we expect to observe a gauss-like function response.
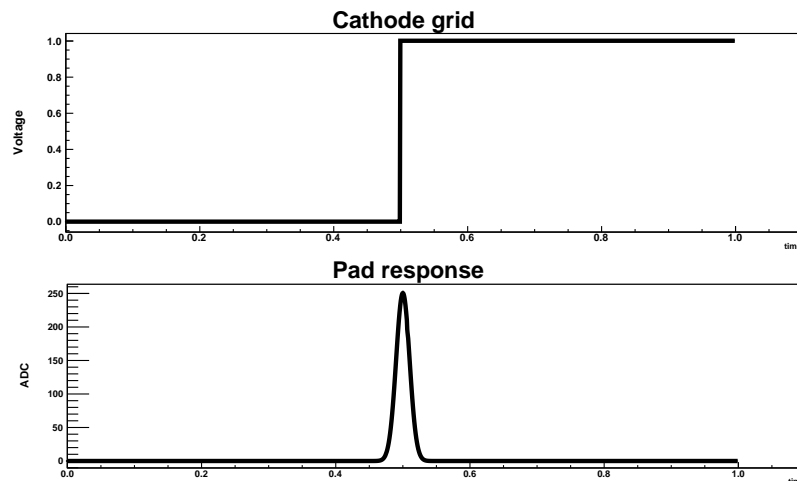
Figure 26: Pulser injects a charge into cathode wires, causing a step function like signal, inducing gaussian-shaped electronic response on the pad plane.

The real pad response is pictured in the plot below. To achieve the highest accuracy we operate in the mode, in which the $51.2\mu s$ time frame is divided into 512 time bins (1 time bin = 100ns). Two issues are necessary to notice:

- After the main peak, we observe an undershoot. This behaviour will be addressed in the next section.

- The peak is four bins (400ns) wide.
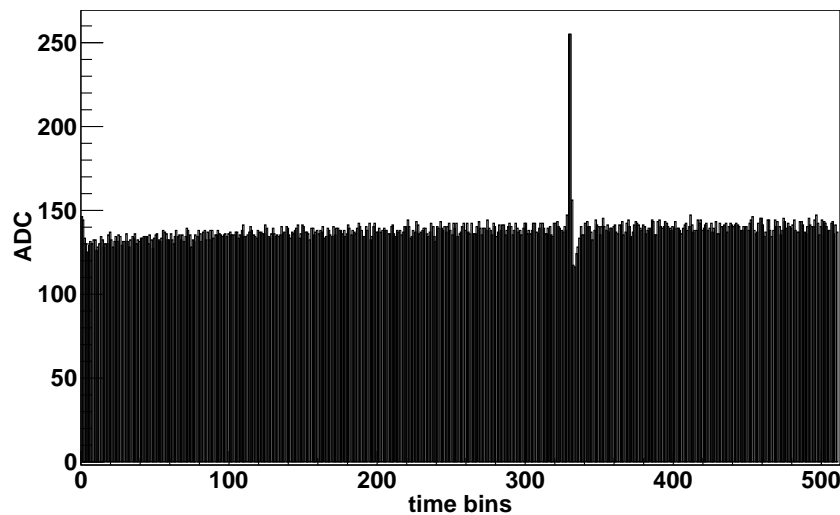
Figure 27: An actual pad response recorded for a pulser signal (1 bin = 100 ns).

400 ns is certainly not the time resolution we want to obtain, since the time variations are the order of tens of ns (compare: **??**). One can think of several methods of improving the precision, e. g. calculation of the center of gravity for such peak. In order to achieve even higher precision

one can perform a function interpolation to the data points. In the next section I will discuss this method in detail, in terms of:

- using a correct fitting function,

- obtaining good fitting parameters,

- implementing the algorithm of interpolation,

- obtaining the lowest uncertainty of peak position.

All the discussion above considered the t_0 time delay calibration. The idea behind the **gain calibration** is much simpler. The electronic gain indicates the strength of a response for an electronic signal. The response intensity calculation in case of pulser would be straight away – it is the height of the peak recorded by the pad.

8 Calibration algorithm

The crucial part of the calibration is the algorithm implemented in the `t0calibration.cc` routine. In the flowchart on the next page I have showed schematically its most important components. In the following sections I will describe the steps in details, sticking to the program execution sequence.

Input Data

a # of events

b # of data points to fit

c starting values

input data files

(t0calibration.cc)

loop over
events

check the reference pad
(event quality assessment) 1

set the reference
values for each event

fit the gaussian (t_0, gain) 2

loop over
pads &
events

calculate sum over events

calculate standard
deviation & errors 3

create a table of
t_0's and gains 4

Input Data

table of t_0's and gains

(plotting.C)

(print.cc)

plot the maps
of t_0's and gains

find malfunctioning pads 5

(browser)

check the events records
in malfunctioning pads

8.1 Input files

The input data are SHINE `.raw` files, which contain the events' histograms. Each event in `.raw` files consists of electronic readouts for all pads in a given TPC for a time-frame of 512 time bins. One time bin is 100ns wide, giving the total time-frame width of 51.2μs. For each time value there is a corresponding value of the intensity of the electronic response measured in ADC units. Each data files consists of approximately 1000 events for a single detector chamber.

8.2 Execution chain

The extraction of the input files is followed by the loop over events. All faulty events are rejected and for all the others the reference values are set. Having the event accepted, the algorithm dives into loop over pads. For each pad the precise peak position calculation is performed.

8.2.1 Event quality assessment

To make sure that we exclude any corrupted data, which would distort the calibration, the quality assessment is performed – see: 1 .
The event is examined on an arbitrary chosen reference pad (which is known to work correctly). Each pulse histogram is studied in terms of peak position and peak height. There is a signal threshold at the level of 6 ADC and the maximal signal intensity is set at 250 ADC. Therefore when the peak is to small or to high the data loss might occur. It is also most convenient to read the signal in the middle part of the time-frame.
The approximate peak position is determined by finding the largest entry in the histogram (here denoted with: x_0, $y(x_0)$).
Following criteria are being used:

- Peak position: $x_0 \in (70\text{tb} : 430\text{tb})$

- Peak height: $y(x_0) \in (40\text{ADC} : 220\text{ADC})$

If the event gets accepted the peak fitting routine (described below) is executed for the reference pad and the reference values of t_0 and gain are set.

8.2.2 Fitting the function

2 :   The clue of the calibration algorithm is to find the peak position. To ensure the high precision of those calculations, the suitable function must be chosen. In the figure 1 there is a clearly visible undershoot right after the peak. Such a shape suggests, that what we observe is actually a **damped oscillator**. The physics under that function would be a RLC circuit, which oscillations are described with a following function:

$$x(t) = e^{-\gamma t} A \cos(\omega t) \tag{1}$$

where $\omega = \sqrt{\frac{1}{LC} - \left(\frac{R}{2L}\right)^2}$

and $\gamma = \frac{R}{2L}$

Unfortunately we are unable to measure values L and C, so in the fitting routine there is as many as 3 variables:

- A - amplitude,

- γ - damping factor,

- ω - frequency.

And for the computational purposes the equations takes the following form:

$$f(t) = -p + H(t - t_0 + \frac{\pi}{2\omega}) \cdot A \cdot \exp(-\gamma(t - t_0)) \cdot \cos(\omega(t - t_0)) \tag{2}$$

where:

- p – pedestal,

- $H(t)$ – Heaviside function,

- t_0 – position of the peak.

A fitting routine returns the t_0 value with an χ^2 error estimation of:

$$\mathrm{err}(t_0) > 0.5 \cdot \text{time bins}$$

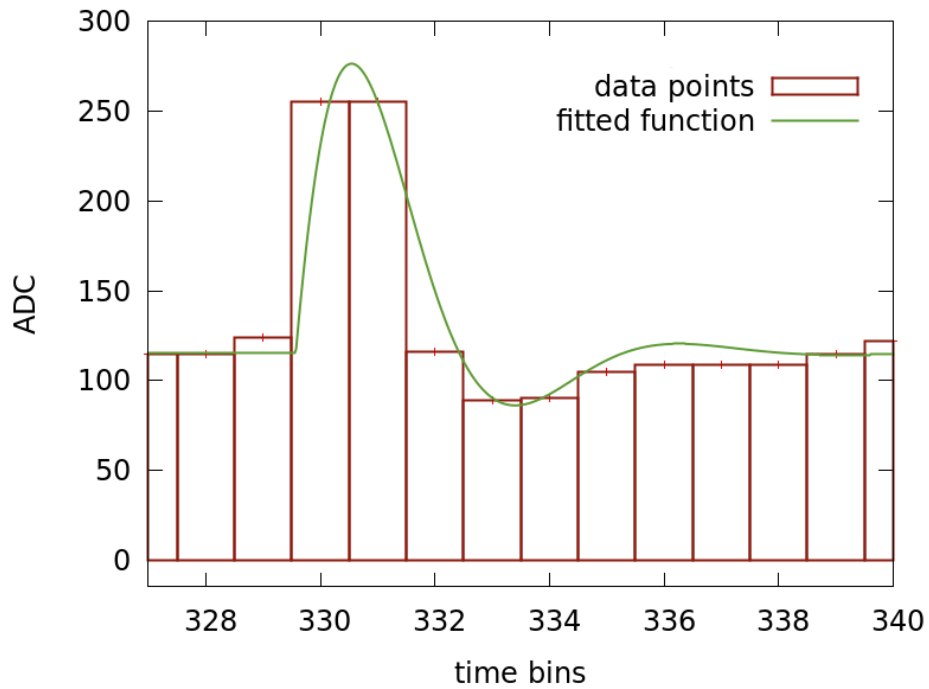This is a not satisfying value for precise calibration of the TPCs.

Figure 28: Fitting result for a damped oscillator function.

We can judge by eye, that the choice of the damped oscillator function was rather poor. There is no possible way of stretching the function so it would match the data points.

The more proper choice as a fitting function turned out to be the gaussian function, when used for pedestal subtracted data.

$$f(t) = A \cdot \frac{1}{\sqrt{2\pi}\sigma} \cdot \exp\left(\frac{-(t - t_0)^2}{2\sigma^2}\right) \tag{3}$$

- σ^2 – variance parameter,

- t_0 – position of the peak,

- A – amplitude.

Now the only fit parameter is t_0. Variance σ^2 can be approximated very well using the reference data for each TPC. And the amplitude A can be extracted by summing the bins' values:

$$A = \sum_{i=-2}^{2} y_i \cdot \Delta t$$

where index i refers to the t coordinate and is equal 0 for the highest bin and Δt is simply 1 time bin. To avoid taking into account any noisy bins, I am summing only 2 bins from each side.
Such an approach ensures that all the points in the peak are included in the calculation, not only the highest one.

For Levenberg-Marquardt algorithm it is essential to properly choose the starting point t_0. A quick non-iterative approach can be used – the center of gravity calculation:

$$t_0 = \frac{\sum_{-2}^{2} y_i \cdot t_i}{\sum_{-2}^{2} y_i}$$

Again there are only 5 points used for simplicity and error reduction.
Fitting routine χ^2 uncertainty decreased up to:

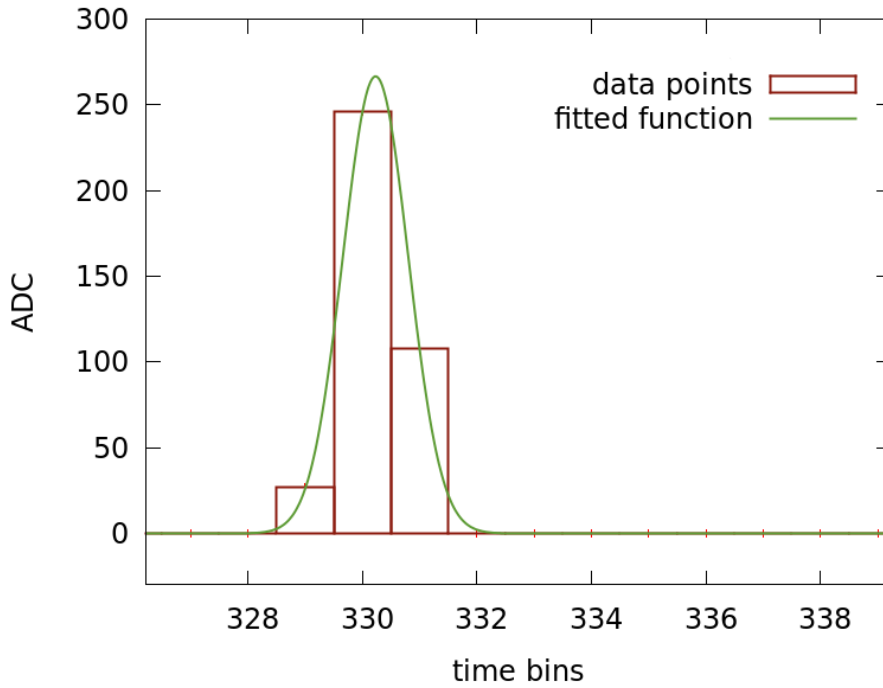$$\mathrm{err}(t_0) < 0.01 \cdot \text{time bins}$$

Figure 29: Fitting result for a gaussian function.

Now coming back to the calibration – I perform such fitting for each event and each pad. During the loop execution I fill out following two multidimensional arrays:

- `t0`   `[# of sectors] [# of pad rows] [# of pads] [# of events]`   – $t_n^{i,j,k}$

- `gain` `[# of sectors] [# of pad rows] [# of pads] [# of events]`   – $g_n^{i,j,k}$

8.2.3   Averaging loop and error calculation

3️⃣   Using the data in arrays `t0` and `gain` we can obtain the average values and statistical errors. We use the value N, which is the number of actually processed events: $N =$ ⓐ - (# of faulty events).

$$\bar{t}^{i,j,k} = \sum_{n=1}^{N} t_n^{i,j,k} \,/N, \qquad \bar{g}^{i,j,k} = \sum_{n=1}^{N} g_n^{i,j,k} \,/N \tag{4}$$

$$\sigma(t^{i,j,k}) = \sum_{n=1}^{N} \left(t_n^{i,j,k} - \bar{t}^{i,j,k} \right)^2, \qquad \sigma(g^{i,j,k}) = \sum_{n=1}^{N} \left(g_n^{i,j,k} - \bar{g}^{i,j,k} \right)^2 \tag{5}$$

Which leads to statistical errors:

$$\Delta t^{i,j,k} = \sqrt{\frac{1}{N(N-1)}} \cdot \sigma(t^{i,j,k}), \qquad \Delta g^{i,j,k} = \sqrt{\frac{1}{N(N-1)}} \cdot \sigma(g^{i,j,k}) \tag{6}$$

Values $t^{i,j,k}$ and $g^{i,j,k}$, along with their statistical errors, are printed to the text file 4️⃣ and in such form may be used in the experiment's calibration chain.

8.3 Hunter of the broken pads

There is an additional side-quest to be performed by the calibration algorithm. The array of time delays, gains and uncertainties can be further used for seeking of malfunctioning pads. In the table below we can see a sample of the array, where there are clearly visible deviations from the usual values. I purposely present a noisy spot, with all kinds of unexpected behaviour.

sector	row	pad	t_0	$\Delta(t_0)$	gain	$\Delta(\text{gain})$
2	8	97	0.111782	0.001732	0.182982	0.001636
2	8	98	0.104289	0.001653	0.182710	0.001538
2	8	99	43.344959	7.474942	0.023477	0.000921
2	8	100	0.089701	0.002146	0.127037	0.001211
2	8	101	0.106981	0.001676	0.185529	0.001430
2	8	102	0.100929	0.001656	0.184514	0.001396
2	8	103	0.106047	0.001684	0.191033	0.001528
2	8	104	0.114349	0.001588	0.176218	0.001364
2	8	105	0.105992	0.001635	0.176943	0.001329
2	8	106	0.100031	0.001635	0.162913	0.001400
2	8	107	0.092971	0.001780	0.157671	0.001536
2	8	108	0.086066	0.001933	0.143345	0.001368
2	8	109	0.074481	0.002100	0.129026	0.001304
2	8	110	0.061871	0.002711	0.109895	0.001414
2	8	111	-139.645059	11.050293	1.324451	0.030559
2	8	112	-308.151203	1.514833	1.705231	0.046734
2	8	113	-0.155059	0.002297	0.197712	0.001688
2	8	114	536719978.157960	0.006745	0.000000	0.000000
2	8	115	-0.162712	0.002277	0.191897	0.001605
2	8	116	-0.148796	0.002189	0.192297	0.001590
2	8	117	-0.102980	0.002018	0.196162	0.001778
2	8	118	-0.144312	0.002157	0.181372	0.001436
2	8	119	-0.144205	0.002213	0.180879	0.001544

Figure 30: Short fragment of the table of calibration factors with visible deviations in values.

We can observe four different kinds of suspiciousness in the array:

- high absolute t_0 value,

- high value of $\Delta(t_0)$,

- gain and $\Delta(\text{gain})$ equal 0.

Setting a cut-off value for $\Delta(t_0)$ seems the most convenient way of finding faulty pads. Unfortunately pads like nr 114 occur frequently, so there is a necessity to add another criterion,

judging gains or t_0s.

The criteria used in my algorithm are as follows – mark as faulty if:

- $\Delta(t_0) > 0.01 \mathrm{tb}$

- $|t_0| > 10$

Part III

Results

9   Output

This section is devoted to picturing some of the results of the pulser calibration. Closer attention will be paid to the details, which allow quality assessment of the calibration results. I will look into the output values, observed repeating patterns and statistical errors. Also if anything went wrong – it should manifest itself on the plots I present in next sections.

9.1   Time delays factors

Following pictures (Fig. 31 and Fig. 32) are enclosed to give an idea of actual timing discrepancies among pads. The Gap-TPC, pictured directly below, consists of only one sector. One of the properties is quickly catching the eye – pads are grouped in an amount of 16. There is a significant values difference between the one-chip group, while the discrepancies within the group are usually an order of magnitude smaller. That is exactly what was expected (see: section 7.3), indicating the correctness of obtained results.
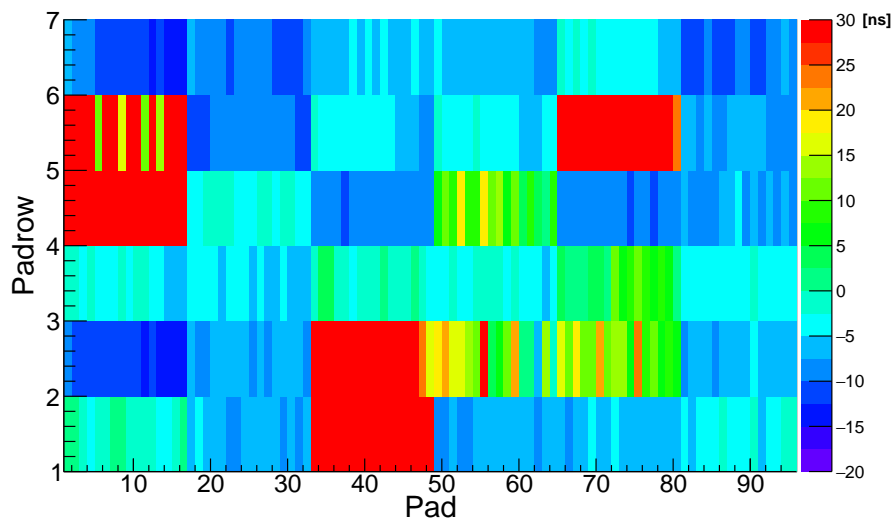

Figure 31: Time delays for GTPC. The colour-scale palette shows values between -20ns and 30ns.

For a bigger scale comparison six sectors of VTPC-1 are presented. Again coupling by 16 is noticeable. The time delay diversity among pads reaches tens of nanoseconds. In the sectors 2 and 5 one can notice a vivid division – it is due to the fact, that in those two sectors there are narrower pads from the side of the target.
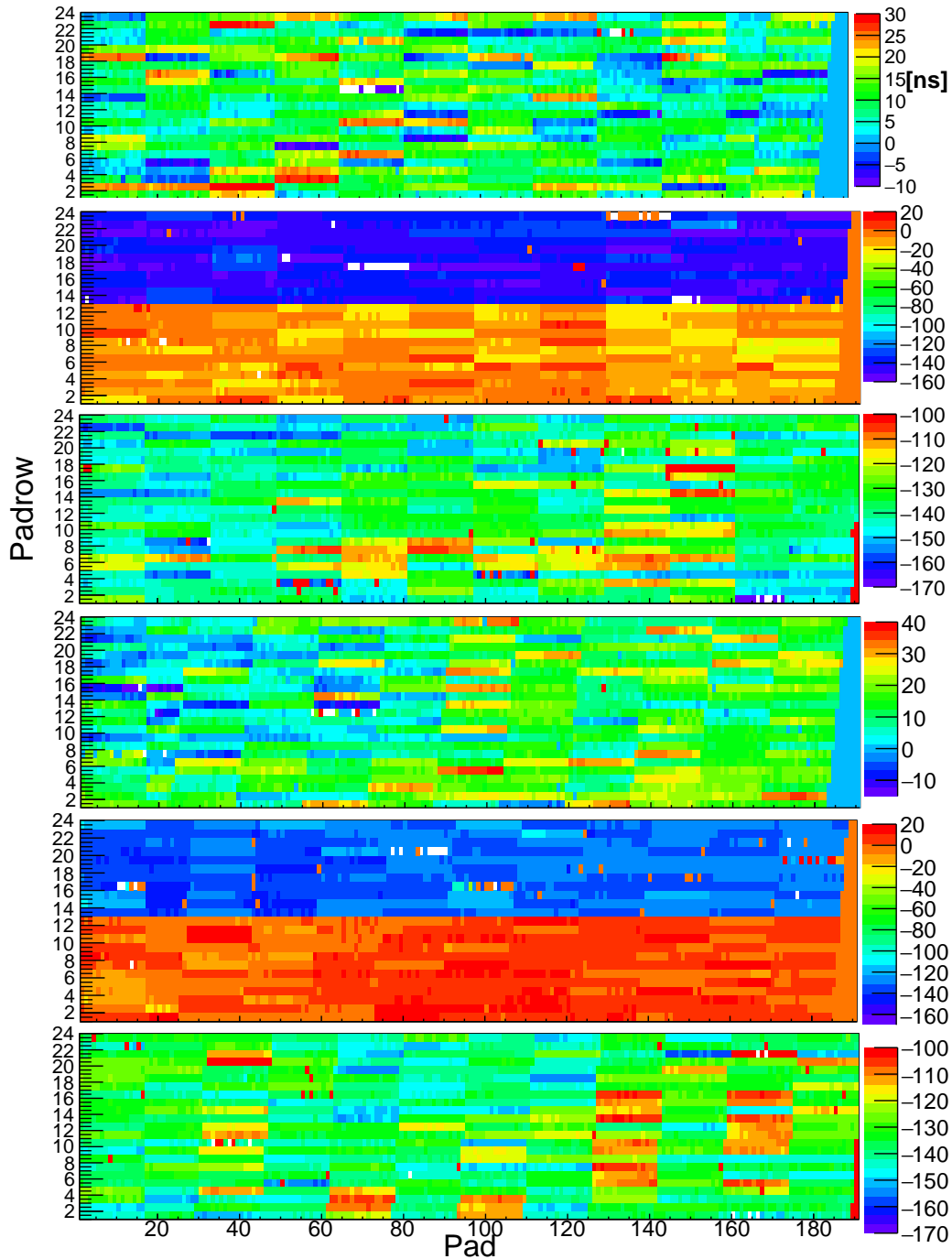

Figure 32: Time delays for VTPC-1. Units of pictured values are nanoseconds.

9.2 Time delays uncertainty

It can be seen straight away in the picture below, that in most cases statistical uncertainties fall below one nanosecond. The errors for VTPC-2 are significantly larger. It is most probably due to some minor fault in pulser electronics, but it will be know for sure only after further hardware analysis.
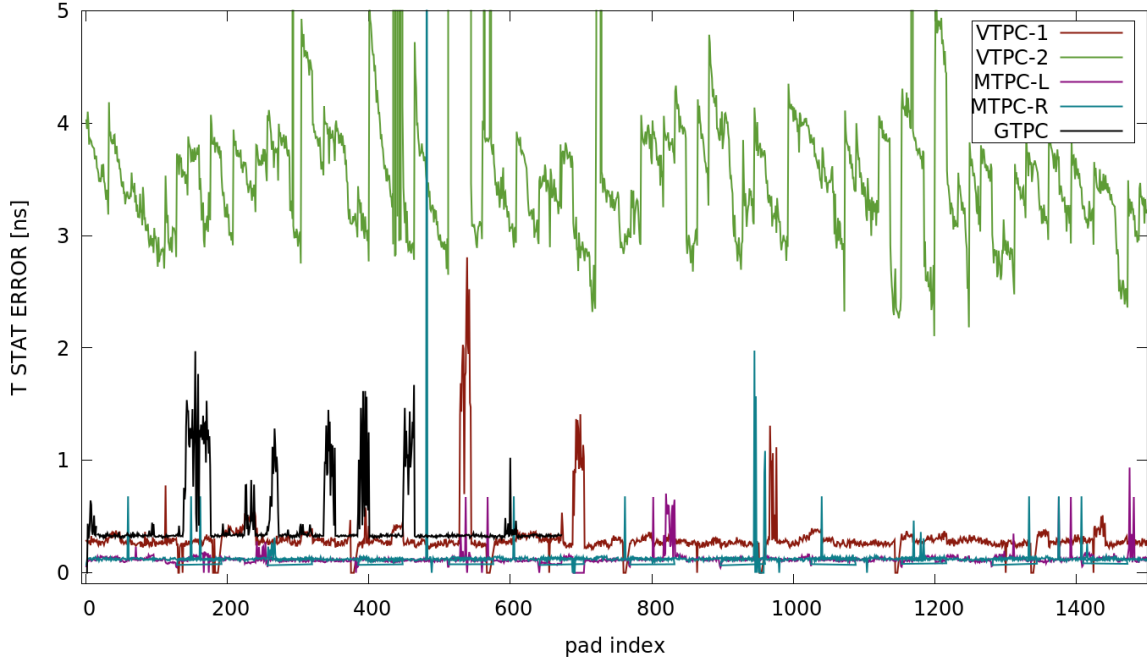

Figure 33: Statistical uncertainties of calculated time delays (in nanoseconds). The values for malfunctioning pads (see section 8.3) were omitted, since they dimmed the picture.

In any case the results are satisfactory. A brief explanation of that statement goes as follows: spatial resolution in a xz-plane is approximately set by the dimensions of pads, which are:

$$\Delta x \approx 3.5mm, \quad 3.6mm, \quad 4.0mm, \quad 5.5mm$$
$$\Delta z \approx 16mm, \quad 28mm, \quad 40mm$$

In calculation of y-resolution we will assume, that its main uncertainty factor will depend on the timer precision, which will in fact be the time delay uncertainty pictured in the plot above. We conclude that 1ns of timer error causes a following uncertainty of y coordinate calculation:

$$\Delta y \approx [\text{drift velocity}] \times [\text{timer error}] = \begin{cases} 1.4 \ cm/\mu s \quad \cdot \quad 1 \ ns \quad = \quad 0.014 \ mm \\ 2.3 \ cm/\mu s \quad \cdot \quad 1 \ ns \quad = \quad 0.023 \ mm \end{cases}$$

Considering so tiny factors we can safely state, that the time delay calibration is performed with a satisfactory precision.

9.3   Gain factors

Gain factors are unit-less values describing an electronic gain relative to an arbitrary chosen reference pad. One can notice in the plot below, that discrepancies in gains are actually significant and may reach even 100%.
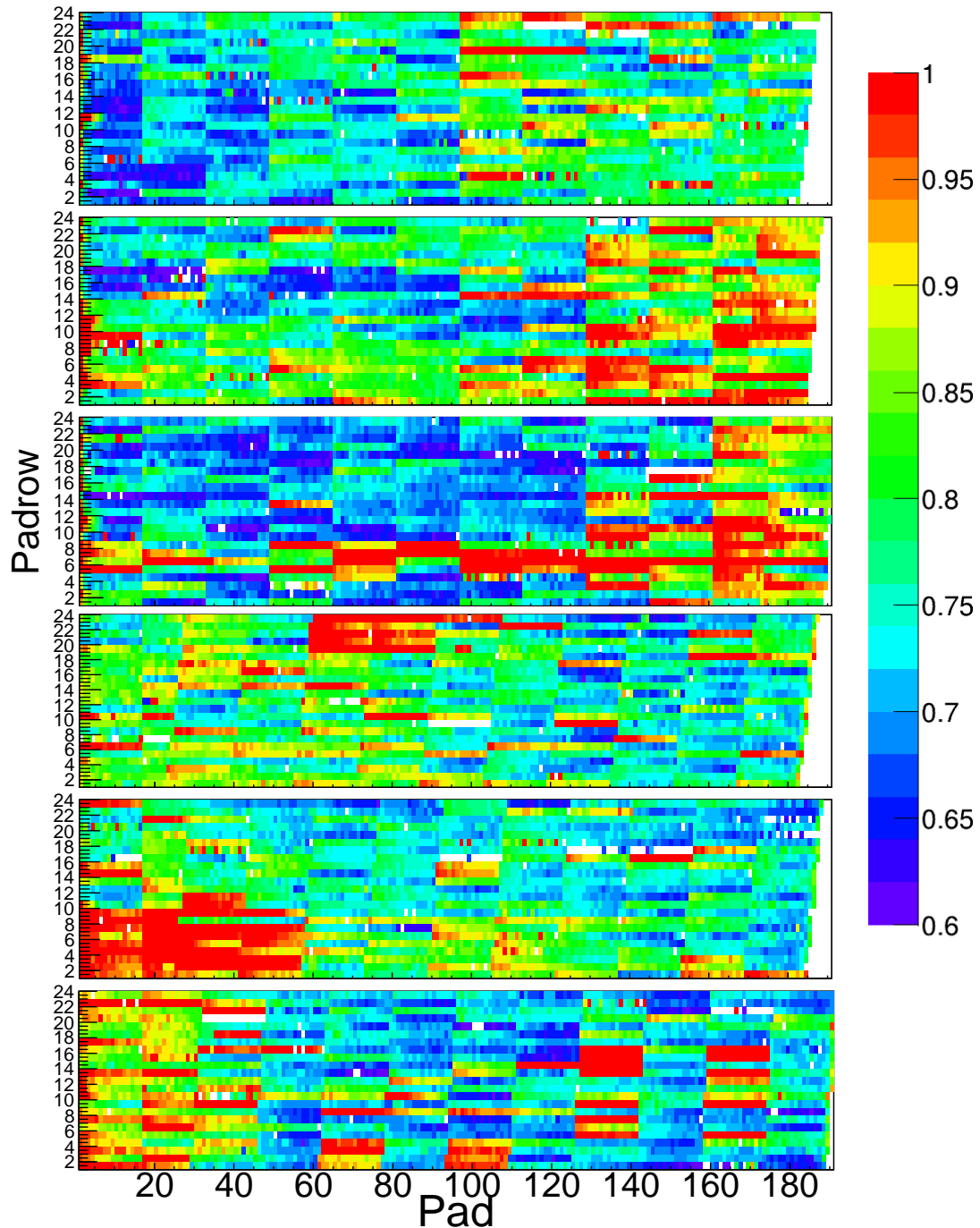

Figure 34: Gain factors for VTPC1. Large spread of values is noticeable, as well as the fact, that pads are grouped by 16.

9.4 Gain uncertainty

Pulser tool in NA61/SHINE was never aimed to measure pad-by-pad gains. Its main purpose is the t_0 calibration. Anyway, one can try to hit two birds with one stone and measure the gains as well. Results are carrying surprisingly low statistical errors, as seen in the plot below.
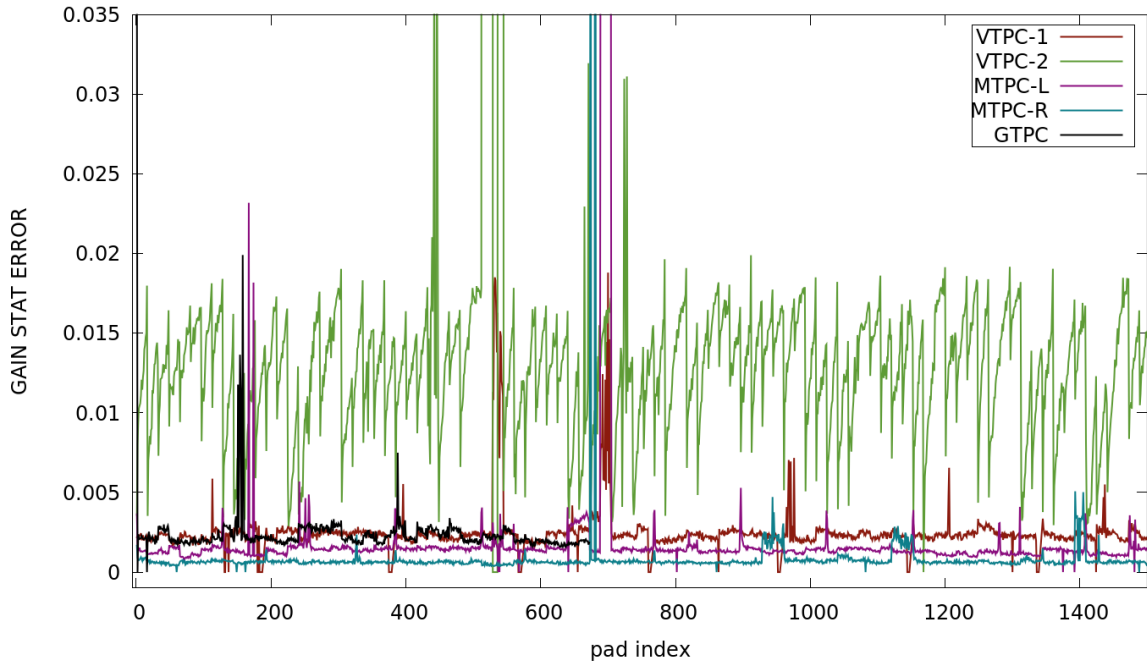

Figure 35: Statistical uncertainties of calculated relative gain factors. The values for malfunctioning pads (see section 8.3) were omitted here as well.

Naturally the question arise whether such results are trustworthy. That matter will be further discussed in the section 10.

9.5 Malfunctioning pads

The analysis of obtained gain and time delay factors may be used to determine which of the pads should be excluded from data acquisition and marked as malfunctioning. Detailed analysis, described in section refsec:malf revealed following amounts of broken pads in each TPC:

- MTPC-L: **318** broken pads, $\approx 0.50\%$

- MTPC-R: **496** broken pads, $\approx 0.78\%$

- VTPC-1: **339** broken pads, $\approx 1.25\%$

- VTPC-2: **472** broken pads, $\approx 1.71\%$

- GTPC: **1** broken pad, $\approx 0.15\%$

Summing up: there is 1626 broken pads out of 182784 total ($\approx 0.9\%$). In VTPCs we observe the largest fraction, while in newer GTPC there is just one broken pad, according to the calibration results. As an example, in the picture below, I plotted a distribution of all malfunctioning pads in MTPC-L. In some cases the pads are grouped by 16, which would indicate, that the whole chip is down.
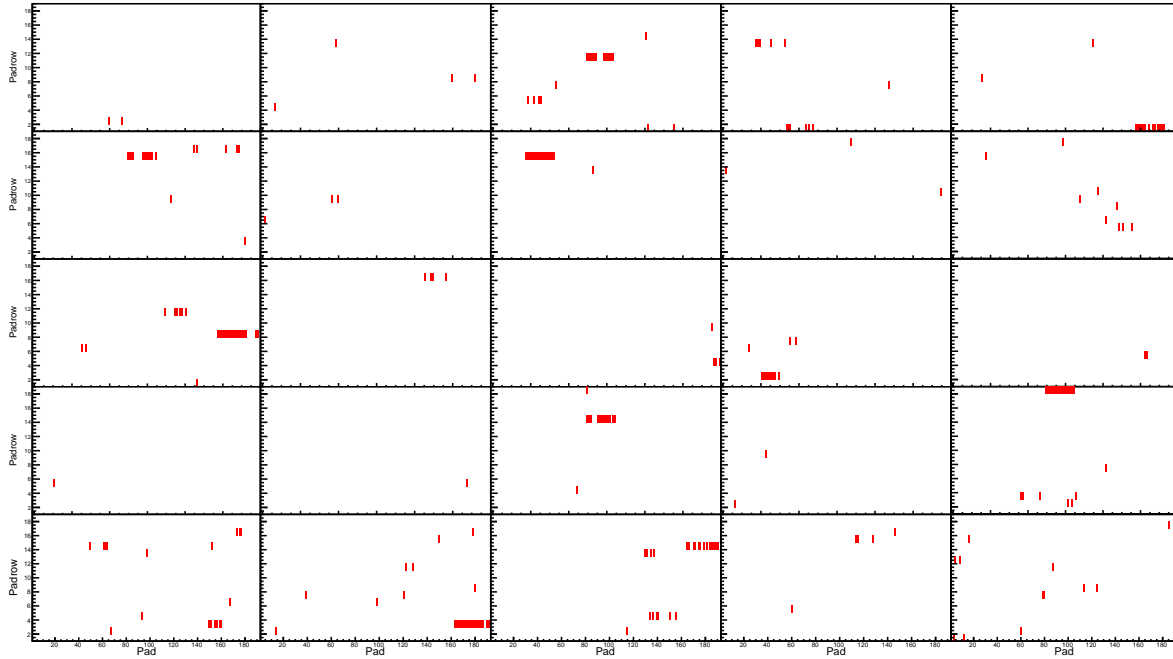

Figure 36: Malfunctioning pads in MTPC-L. We can see that in some cases the whole chip (16 pads) is faulty.

9.6   Calibration performance

The important factor of the calibration is its computational complexity. The more events are analyzed, the lower the statistical uncertainty gets. But on the other hand for a larger quantities of events the computational time rises as well as the resources consumption. The sufficient number of processed events in terms of the statistical error is the order of 100.

As an example of execution performance I would use the MTPC-L calibration with 100 events analyzed:

Processor resources:	2.4 GHz (single threaded)
Execution time:	9min 34s
RAM usage (virtual):	443.3MB (710.0MB)

The execution time for mentioned parameters is satisfactory. There is no desperate need to parallelize the algorithm or reduce the memory consumption. The execution time grows linearly with the number of events. The linear growth with event number is also the case for the RAM usage.

10 Comparison against the Krypton calibration

As was already said before, the pulser calibration was aimed to obtain the t_0 delays. Gain factors were only a secondary task. A fact, also discussed before, is that the pulser gain output comes with a very low statistical uncertainty ($<1\%$). The pulser obtains gain factors in a completely different way than the TPCs operate during measurements. The pulser causes a pad response through an electromagnetic induction. TPCs on the other hand, operate collecting charged particles, so in fact the chambers collect an actual charge. Such a difference in the approach tells us to question, whether the pulser gain factors are as reliable, as the ones obtained with a decaying krypton.

The sections below address that question through a comparison of results of both calibrations.

10.1 Krypton calibration procedure

One way to obtain a good calibration data is to resemble the standard detector operation, but in well controlled and well quantified way. The idea is to inject a chamber with radioactive $^{83}_{36}\mathrm{Kr}$ isotope. The deexcitating Krypton produces photons with an energy high enough to create free electrons via the photo-electric effect in the interaction with chamber gas molecules. The electrons are then drifted towards the pad plane.

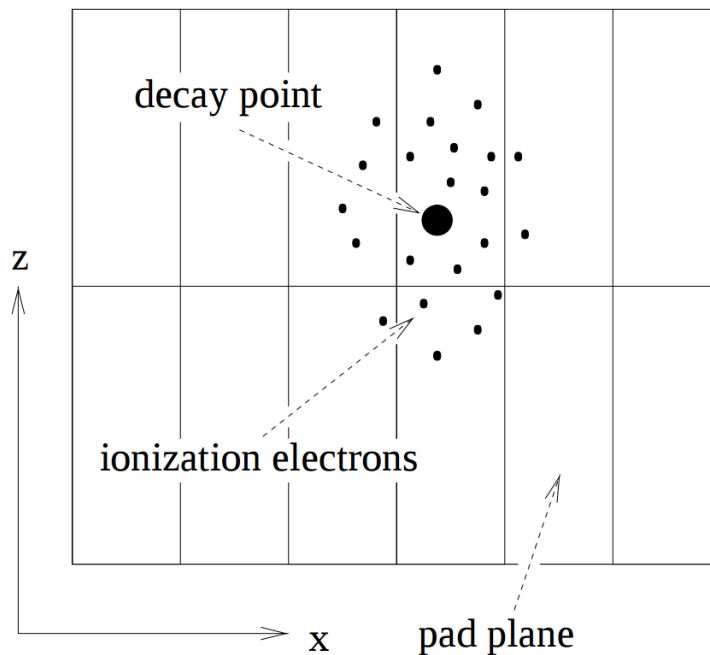Figure 37: Krypton decays in the TPC chambers causing secondary ionization, arriving later at a pad plane.
image credit: [12]

In the plot below we can see the characteristic $^{83}_{36}\mathrm{Kr}$ decay energy spectrum obtained with a Monte Carlo simulation. The simulation took into account the effects of the chamber gas surrounding Krypton, which is why the peaks are not sharp, but scattered wide.
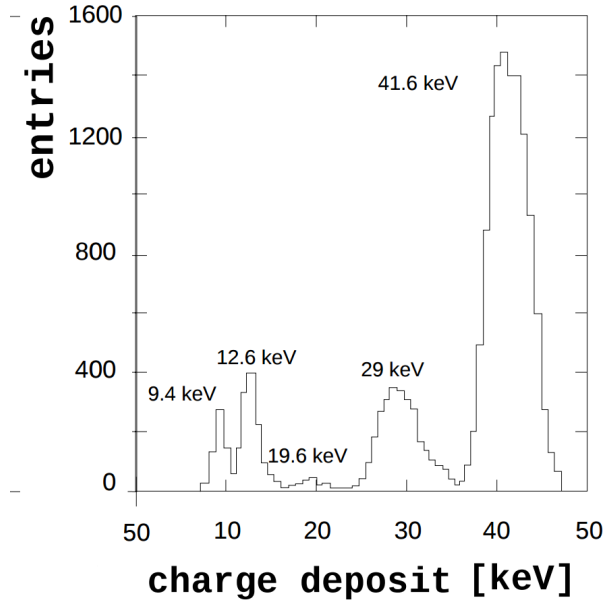
Figure 38: Krypton decay energy spectrum. The shown plot is a result of a Monte Carlo simulation, which has taken into account the detector environment effects.
image credit: [12]

The corresponding quantity measured by the TPC is the total charge – the number of electrons created in the ionization is proportional to the energy, that caused the ionization. Following such logic we expect to see the resembling shape of spectrum in the plot of the number of counts versus the total charge (see the plot below). We collect a huge number of events to improve the spectrum shape and reduce the errors. The next step is to fit the gaussian function to the highest peak. The total charge for which we observe a maximum of the peak is then used directly as a comparable gain factor.
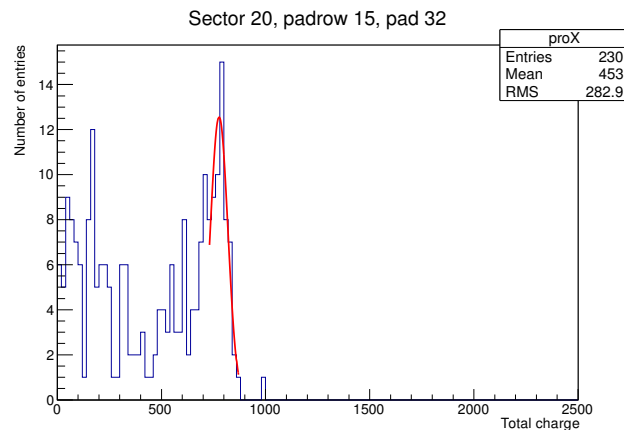

Figure 39: To determine the peak position with the highest precision we fit the gaussian function to the histogram and we treat the function maximum as the precise peak position.
image credit: Michał Naskręt

10.2   Gain comparison

The plots presented below show the gain factors obtained by both calibrations. One can judge by eye, that there surely is a qualitative consistency of results. One (and probably only) conclusion, that can be drawn, is that both of the calibration approaches seem to prove themselves approximately correct.
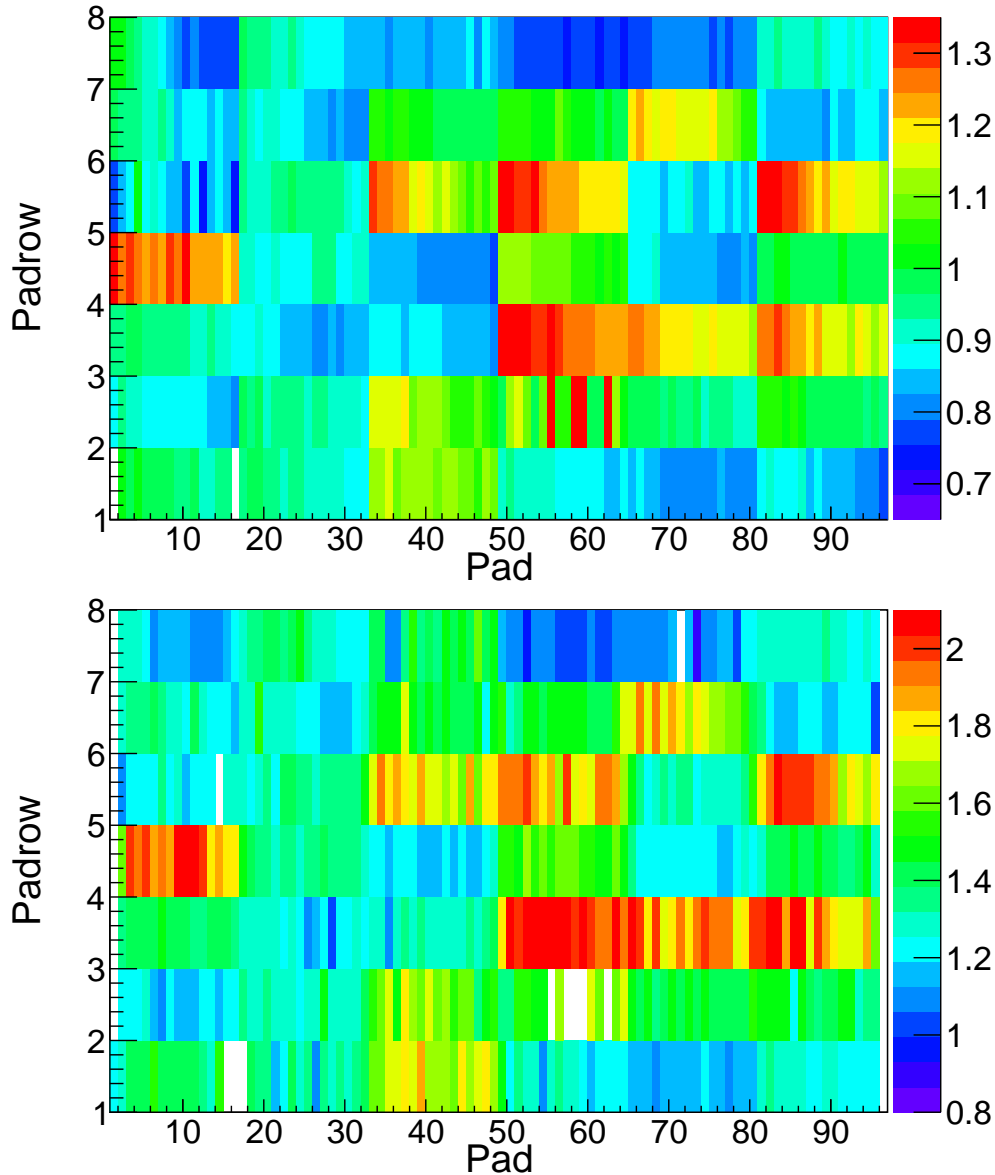
Figure 40: Comparison of gain factors obtained by two different methods: pulser (top) and krypton (bottom) calibration. One can judge by eye, that there is a good agreement of those two methods. The difference in absolute values comes from a different selection of a reference pad.

In order to judge the results in a quantitative way, I present below a histogram plot. One can notice straight away, that the values for Krypton are usually higher that ones for the pulser. The reason for that is most probably a leak of charge to adjacent pads and padrows.

The discussion about whether the pulser gain factors are reliable is currently ongoing. The conclusion at the moment is as follows – the pulser gain factors cannot be fully trusted, but might serve very well for two tasks:

- gain factors change over time – it is much less complicated and much quicker to record pulser data than Krypton,

- pulser factors might will prove useful as starting values for Krypton calibration.
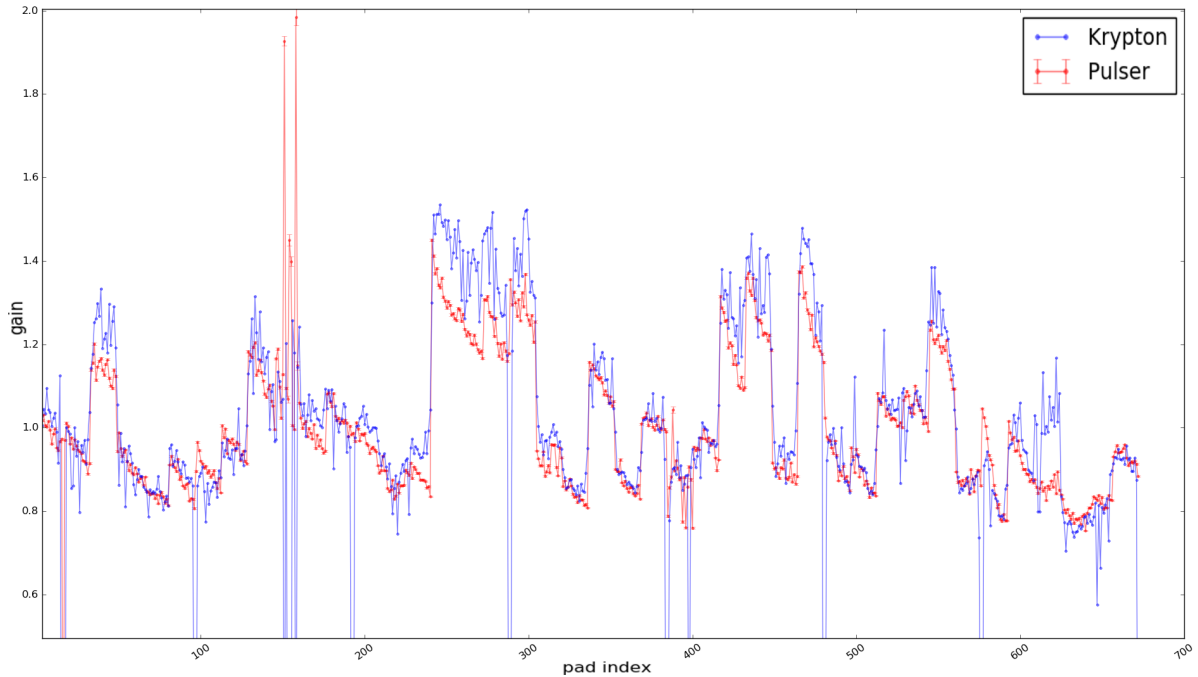
Figure 41: Again a comparison of gain factors obtained by two different methods: pulser and Krypton calibrations for GTPC. In this case all the values were normalized – scaled by dividing by an average value.

10.3 Faulty pads

Plots below show the pads in VTPC-1 (serving as an example) pointed out as malfunctioning by pulser and Krypton calibrations. First thing to notice is significantly larger number of faulty pads according to the Krypton. The method of determining bad pads in case of the pulser was presented in detail in section 8.3. For a Krypton calibration faulty pads are the ones, for which the algorithm failed to found a peak maximum in a given range.

Figure 42: The pads listed as malfunctioning by pulser (top) and krypton (left) calibration in all six sectors of VTPC-1. A noticeable property is that krypton calibration points out significantly more pads to be broken.

Quantitatively those are the differences in the numbers of broken pads found with two described approaches:

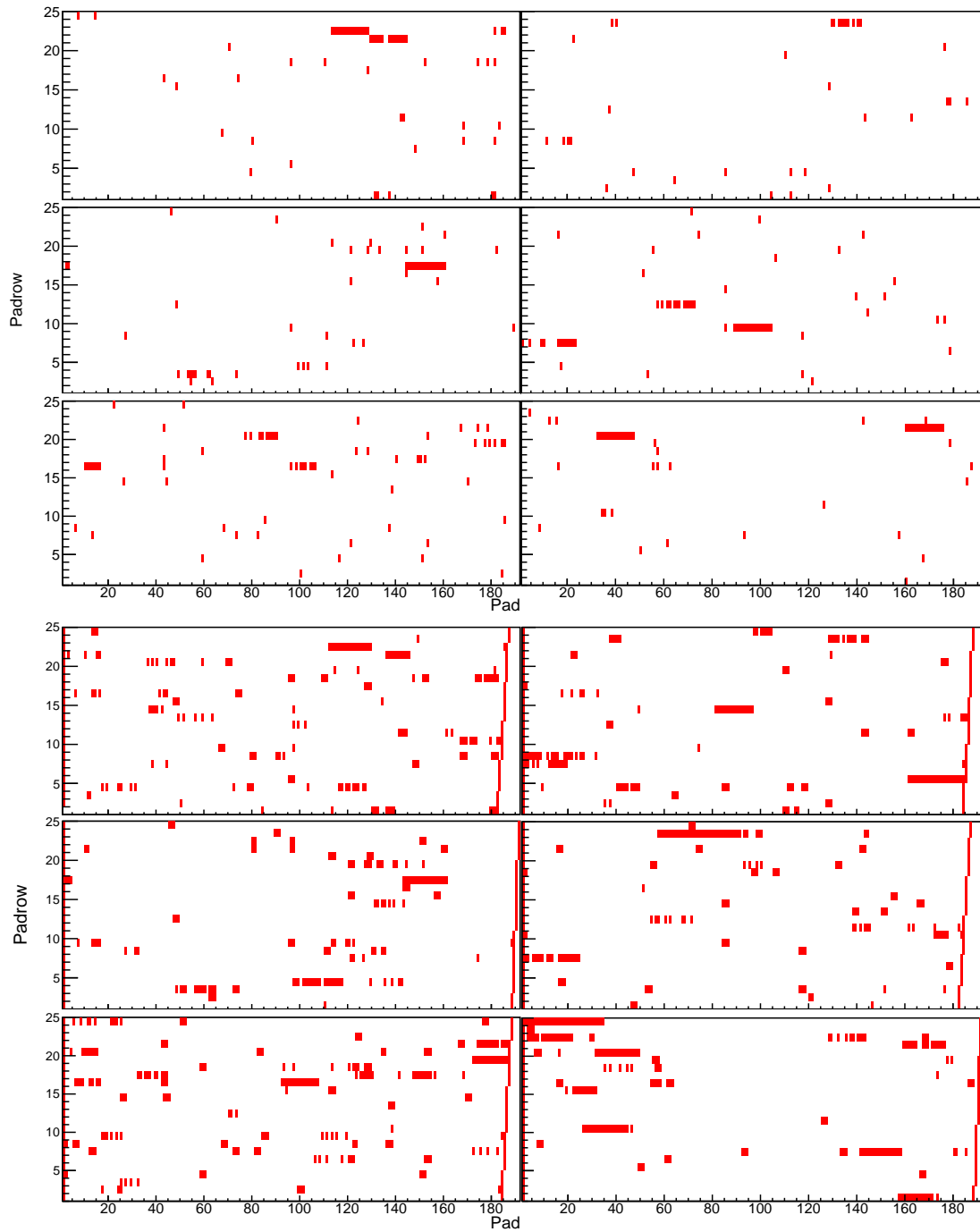|	Malfunctioning pads:	Percentage:
Krypton calibration	1383	$\approx 5.14\%$
Pulser calibration	339	$\approx 1.25\%$

In this case pulser approach seems as more robust. It has clearly defined constraints and in a quick way one can check what is the actual signal structure for a given pad. In case of Krypton calibration, the task is more complicated and there is no easy way to estimate the reliability of the broken pad hunter.

Part IV

Summary

What I present in this thesis, is a complete description of the TPC calibration procedure using a pulser tool. It consists of a detailed depiction of the algorithm and hardware setup. I pictured how this work fits in the NA61/SHINE collaboration as a whole and I provided a thorough analysis of obtained results.

The final product for the experiment is a robust, well-tested code fitting in SHINE Offline framework and the map of t_0 time delays and gain factors pad-by-pad for each of the TPCs. Those correction factors are calculated with satisfactory low uncertainties and may be trustworthy used in the data analysis chain, improving the data quality.

Despite of the calibration being finished, one can think of some possibilities of extending the research in this subject. First of possible ways to continue, is to study the aging of the detector electronics, using both historical and newly recorded data. Expected result is observing more malfunctioning pads through aging and possibly changes in the calibration factors. The second idea of continuing the subject is to dive into the differences between gain factors obtained by Krypton calibration and the one described here.

Acknowledgements

I would like to express my gratitude to professor Ludwik Turko, who created a great opportunity for me to join the NA61/SHINE collaboration.

Secondly I want to thank my friend Michał Naskręt, whom I joined the NA61 with and with whom I was working on a countless tasks during our studies.

In the NA61 I have worked with brilliant people, who broadened my scientiffic horizons, who I also want to thank: Dr Andras Laszlo and prof. Marek Gaździcki

Furthermore I give my gratitude to my supervisor Dr Thomas Klähn, for a trouble-free cooperation.

And last but not least I would like to thank my familiy and friends for an endless support and keeping me sane and motivated.

Part V

Appendix

A   Software

This section is devoted to describing the software and algorithms that have been used in the calculations. The whole software project was written in `C++` programming language with an addition of SHINE Offline framework and Gnu Scientific Library. The analysis of the results was performed with a usage of root, gnuplot and python's matplotlib.

A.1   Gnu Scientific Libraries

Gnu Scientific Library (GSL) is a library for numerical calculations in C and C++. The license of GSL is a free one, under GNU General Public License. The library consists of numerous mathematical routines concerning a wide variety of topics: number generators, special functions or fitting.

The version used in this thesis is a GSL-1.16, released in July 2013. GSL package is well know as reliable, robust and fast numerical package.

A.1.1   Levenberg-Marquardt algorithm

Levenberg–Marquardt algorithm is an iterative, nonlinear optimization algorithm. Given the series of data $(t_i, y_i) \in \mathbf{R}^2$, where i iterates from 1 to N. We are looking for a configuration minimizing the function:

$$\chi^2(\mathbf{p}) = \sum_{i=1}^{N} [y_i - f(t_i, \mathbf{p})]^2,$$

where $\mathbf{p}$ is the vector of parameters. This can be reformulated to a general form – optimization of nonlinear function:

$$\Phi(\mathbf{x}) = \frac{1}{2} \sum_{i=1}^{N} r_i^2(\mathbf{x}), \qquad \Phi(\mathbf{x}) = \|\mathbf{r}(\mathbf{x})\|^2$$

Now the $\mathbf{x}$ is a vector in $\mathbf{R}^n$, χ is substituted by a residual vector – $\mathbf{r}(\mathbf{x}) = (r_1(\mathbf{x}), \ldots, r_N(\mathbf{x}))$. Differentials of $\Phi(\mathbf{x})$ may be expressed as a Jacoby matrix: $\{\mathsf{J}(\mathbf{x})\}_{ij} = \frac{\partial r_i}{\partial x_j}(\mathbf{x})$

Now we can denote the gradient of function Φ as:

$$\nabla\Phi(\mathbf{x}) = \sum_{i=1}^{N} r_i(\mathbf{x})\nabla r_i(\mathbf{x}) = \mathsf{J}(\mathbf{x})^{\mathsf{T}}\mathbf{r}(\mathbf{x})$$

And this would give us a following Hessian:

$$\nabla^2\Phi(\mathbf{x}) = \mathsf{J}(\mathbf{x})^{\mathsf{T}}\mathsf{J}(\mathbf{x}) + \sum_{i=1}^{N} r_j(\mathbf{x})\nabla^2 r_j(\mathbf{x}) \approx \mathsf{J}(\mathbf{x})^{\mathsf{T}}\mathsf{J}(\mathbf{x})$$

The easiest iterative approach to minimization of Φ function is described with a scheme:

$$\mathbf{x}_{i+1} = \mathbf{x}_i - \lambda \nabla \Phi(\mathbf{x}_i)$$

However, this method is slow. To improve the performance we can use our knowledge about the second derivative. Being exact, we will use the function Taylor expansion up to the second order:

$$\nabla \Phi(\mathbf{x}) = \nabla \Phi(\mathbf{x}_0) + (\mathbf{x} - \mathbf{x}_0)^\mathsf{T} \nabla^2 \Phi(\mathbf{x}_0) + \dots$$

This way we end up with a method called *Gauss-Newton* method:

$$\mathbf{x}_{i+1} = \mathbf{x}_i - (\nabla^2 \Phi(\mathbf{x}_i))^{-1} \nabla \Phi(\mathbf{x}_i)$$

Where for the Φ hessian the given approximation is enough.

Kenneth Levenberg proposed a merger of two described approaches, together with an iteration algorithm:

$$\mathbf{x}_{i+1} = \mathbf{x}_i - (\mathsf{H}(\mathbf{x}_i) + \lambda \mathsf{I})^{-1} \nabla \Phi(\mathbf{x}_i)$$

1. Calculate $\mathbf{x}_i + 1$

2. Calculate the estimation error at $\mathbf{x}_i + 1$ point.

3. *Case 1:* the error grew $\rightarrow$ multiply λ k-times and go to point 1.
   Case 2: the error decreased $\rightarrow$ divide λ k-times.

Typically one takes $k = 10$. In case of high λ, the algorithm almost ignores the hessian. Donald Marquardt noticed here a space for improvement:

$$\mathbf{x}_{i+1} = \mathbf{x}_i - (\mathsf{H}(\mathbf{x}_i) + \lambda \operatorname{diag}[\mathsf{H}])^{-1} \nabla \Phi(\mathbf{x}_i),$$

where:

$$\operatorname{diag}[\mathsf{H}] = \begin{bmatrix} h_{11} & 0 & \dots & 0 \\ 0 & h_{22} & \dots & 0 \\ \vdots & \vdots & \ddots & \vdots \\ 0 & 0 & \dots & h_{nn} \end{bmatrix}.$$

Such a correction results with a rapid convergence comparing to any other method. The most costly operation is inverting the matrix, but anyway it is quicker than casual gradient method up to the number of hundreds parameters.

A.2 SHINE Offline Framework

SHINE Offline Framework is a standalone C++ program for NA61 offline purposes. It consists of a framework, a detector description, input methods and a set of event processing modules. The large scale structure of SHINE involves categories listed below:

- UTILITIES
  A set of helper tools, such as: physical unit handlers, coordinate converters, linear algebra and other mathematical tools, etc. Many of them were inherited from the Offline framework of Pierre Auger Observatory.

- DETECTOR AND MANAGERS
  Under this category there are mostly programs providing description of subdetectors. Also the target configuration, beam properties, magnetic field properties, trigger settings etc. are included, as well as I/O modules.

- EVENT
  Also referred to as SHOE (Shine Offline Event) – stores broad set of information about a physical event. The event data is stored in various levels of complexity – starting from raw files straight from data acquisition system, ending with files containing only the information about vertices, tracks and clusters.

- MODULES
  Modules contain substeps of calibration, reconstruction, analysis and simulation procedures.

- EVENT BROWSER Standalone event display capable of displaying events online and also simulated events.

SHINE might also be used as an external library.

A.3   Data visualization – ROOT and Gnuplot

A.3.1   ROOT

Web page: `root.cern.ch`
The ROOT is a system of analysis tool. It is constructed to handle large amounts of data in an efficient way. Included tools are: visualization and graphics, function fitting, evaluation and statistics. The built-in CINT C++ enables interactive usage of command interpreter, but ROOT can be also used as an external, C++ compatible library.
"The ROOT project was started in the context of the [NA61 predecessor –] NA49 experiment at CERN. NA49 generates an impressive amount of data, about 10 Terabytes of raw data per run. This data rate is of the same order of magnitude as the rates expected to be recorded by the LHC experiments. Therefore, NA49 was the ideal environment to develop and test the next generation data analysis tools and to study the problems related to the organization and analysis of such large amounts of data." — *taken from root.cern.ch*

A.4   Gnuplot

According to the Gnuplot homepage (`gnuplot.info`):
"Gnuplot is a portable command-line driven graphing utility for Linux, OS/2, MS Windows, OSX, VMS, and many other platforms. The source code is copyrighted but freely distributed

(i.e., you don't have to pay for it). It was originally created to allow scientists and students to visualize mathematical functions and data interactively, but has grown to support many non-interactive uses such as web scripting. It is also used as a plotting engine by third-party applications like Octave. Gnuplot has been supported and under active development since 1986."

References

[1] Zsolt Kacso Drupalizing. Na61/shine, December 2014.

[2] M. A. Stephanov. QCD phase diagram: An Overview. *PoS*, LAT2006:024, 2006.

[3] A. K. Chaudhuri. A short course on Relativistic Heavy Ion Collisions. 2012.

[4] Robert D. Pisarski and Frank Wilczek. Remarks on the Chiral Phase Transition in Chromodynamics. *Phys. Rev.*, D29:338–341, 1984.

[5] U. Heller. Recent progress in finite temperature lattice QCD. *PoS*, LAT2006, 2006.

[6] Ian M. Barbour, Susan E. Morrison, Elyakum G. Klepfish, John B. Kogut, and Maria-Paola Lombardo. The Critical points of strongly coupled lattice QCD at nonzero chemical potential. *Phys. Rev.*, D56:7063–7072, 1997.

[7] Marek Gazdzicki, Z Fodor, and G Vesztergombi. Study of Hadron Production in Hadron-Nucleus and Nucleus-Nucleus Collisions at the CERN SPS. Technical Report SPSC-P-330. CERN-SPSC-2006-034, CERN, Geneva, Nov 2006. revised version submitted on 2006-11-06 12:38:20.

[8] Marek Gazdzicki and Mark I. Gorenstein. On the early stage of nucleus-nucleus collisions. *Acta Phys. Polon.*, B30:2705, 1999.

[9] C. Alt et al. Pion and kaon production in central Pb + Pb collisions at 20-A and 30-A-GeV: Evidence for the onset of deconfinement. *Phys. Rev.*, C77:024903, 2008.

[10] Yuichi Oyama. Results from K2K and status of T2K. 2005.

[11] N. Abgrall et al. NA61/SHINE facility at the CERN SPS: beams and detector system. *JINST*, 9:P06005, 2014.

[12] Andrzej Rybicki. *Charged hadron production in elementary and nuclear collisions at 158-GeV/c.* PhD thesis, Cracow, INP, 2002.